

Predictions for the CO emission of galaxies from a coupled simulation of galaxy formation and photon dominated regions

Claudia del P. Lagos¹, Estelle Bayet², Carlton M. Baugh¹, Cedric G. Lacey¹, Tom A. Bell³, Nikolaos Fanidakis⁴, James E. Geach⁵

¹*Institute for Computational Cosmology, Department of Physics, University of Durham, South Road, Durham, DH1 3LE, UK.*

²*Department of Physics, University of Oxford, Denys Wilkinson Building, Keble Road, Oxford OX1 3RH, UK.*

³*Centro de Astrobiología (CSIC/INTA), Instituto Nacional de Técnica Aeroespacial, 28850 Torrejón de Ardoz, Madrid, Spain*

⁴*Max-Planck-Institut fuer Astronomie, Koenigstuhl 17, 69117 Heidelberg, Germany.*

⁵*Department of Physics, McGill University, Ernest Rutherford Building, 3600 Rue University, Montreal, Quebec H3A 2T8, Canada.*

3 March 2022

ABSTRACT

We combine the galaxy formation model GALFORM with the Photon Dominated Region code UCL_PDR to study the emission from the rotational transitions of ^{12}CO (CO) in galaxies from $z = 0$ to $z = 6$ in the Λ CDM framework. GALFORM is used to predict the molecular (H_2) and atomic hydrogen (HI) gas contents of galaxies using the pressure-based empirical star formation relation of Blitz & Rosolowsky. From the predicted H_2 mass and the conditions in the interstellar medium, we estimate the CO emission in the rotational transitions 1-0 to 10-9 by applying the UCL_PDR model to each galaxy. We find that deviations from the Milky-Way CO- H_2 conversion factor come mainly from variations in metallicity, and in the average gas and star formation rate surface densities. In the local universe, the model predicts a CO(1 – 0) luminosity function (LF), CO-to-total infrared (IR) luminosity ratios for multiple CO lines and a CO spectral line energy distribution (SLED) which are in good agreement with observations of luminous and ultra-luminous IR galaxies. At high redshifts, the predicted CO SLED of the brightest IR galaxies reproduces the shape and normalization of the observed CO SLED. The model predicts little evolution in the CO-to-IR luminosity ratio for different CO transitions, in good agreement with observations up to $z \approx 5$. We use this new hybrid model to explore the potential of using colour selected samples of high-redshift star-forming galaxies to characterise the evolution of the cold gas mass in galaxies through observations with the Atacama Large Millimeter Array.

Key words: galaxies: formation - galaxies : evolution - galaxies: ISM - stars: formation - ISM: lines and bands

1 INTRODUCTION

The connection between molecular gas and star formation (SF) is a fundamental but poorly understood problem in galaxy formation. Observations have shown that the star formation rate (SFR) correlates with the abundance of cold, dense gas in galaxies, suggesting that molecular gas is needed to form stars. A variety of observational evidence supports this conclusion, such as the correlation between the surface densities of SFR and ^{12}CO (hereafter CO) emission and between the CO and infrared (IR) luminosities (e.g. Solomon & Vanden Bout 2005; Bigiel et al. 2008). The CO luminosity traces dense gas in the interstellar medium (ISM), which is dominated by molecular hydrogen (H_2). The IR luminosity approximates the total luminosity emitted by interstellar dust, which, in media that are optically thick to ultraviolet (UV) radiation, is expected to correlate closely with the SFR in star-forming galaxies.

In the local Universe, high-quality, spatially resolved CO data show a tight and close to linear correlation between the surface density of the SFR and the surface density of CO emission, that extends over several orders of magnitude and

in very different environments: from low-metallicity, atomic-dominated gas to high-metallicity, molecular-dominated gas (e.g. Wong & Blitz 2002; Leroy et al. 2008; Bigiel et al., 2008, 2011; Schruba et al. 2011; Rahman et al. 2012). This suggests that SF proceeds in a similar way in these different environments. Support for this also comes from the IR-CO luminosity relation, with high-redshift submillimeter galaxies (SMGs) and quasi-stellar objects (QSOs) falling on a similar relation to luminous IR galaxies (LIRGs) and ultra-luminous IR galaxies (ULIRGs) in the local Universe (e.g. Solomon et al. 1997; Scoville et al. 2003; Greve et al. 2005; Tacconi et al. 2006; Evans et al. 2006; Bertram et al. 2007; Bayet et al. 2009a; Tacconi et al. 2010; Genzel et al. 2010; Riechers 2011; Daddi et al. 2010; Geach et al. 2011; Ivison et al. 2011; Bothwell et al. 2012). Bayet et al. (2009a) studied the correlation between different CO transitions and IR luminosity and found that this correlation holds even up to $z \approx 6$.

The CO emission from galaxies is generally assumed to be a good indicator of molecular gas content. However, to infer the underlying H_2 mass from CO luminosity it is necessary to

address how well CO traces H_2 mass. This relation is usually parametrised by the conversion factor, X_{CO} , which is the ratio between the H_2 column density and the integrated CO line intensity. Large efforts have been made observationally to determine the value of $X_{CO(1-0)}$ for the CO(1 – 0) transition, and it has been inferred directly in a few galaxies, mainly through virial estimates and measurements of dust column density. Typical estimates for normal spiral galaxies lie in the range $X_{CO(1-0)} \approx (2 - 3.5) \times 10^{20} \text{ cm}^{-2} / \text{K km s}^{-1}$ (e.g. Young & Scoville 1991; Boselli et al. 2002; Blitz et al. 2007; Bolatto et al. 2011). However, systematic variations in the value of $X_{CO(1-0)}$ have been inferred in galaxies whose ISM conditions differ considerably from those in normal spiral galaxies, favouring a larger $X_{CO(1-0)}$ in low-metallicity galaxies and a smaller $X_{CO(1-0)}$ in starburst galaxies (e.g. Leroy et al. 2007, 2011; Magdis et al. 2011; see Solomon & Vanden Bout 2005 for a review).

Theoretically, most studies of X_{CO} are based on Photon Dominated Region (PDR; e.g. Bell et al. 2006) or large velocity gradient (LVG; e.g. Weiß et al. 2005) models. Such models have been shown to be an excellent theoretical tool, reproducing the emission of various chemical species coming from regions where the CO emission dominates (i.e. in giant molecular clouds, GMCs, where most of the gas is in the atomic or molecular phase, with kinetic temperatures typically below 100 K, and densities ranging from 10^3 cm^{-3} to 10^5 cm^{-3}). These models have shown that X_{CO} can vary considerably with some of the physical conditions in the ISM, such as gas metallicity, interstellar far-UV (FUV) radiation field and column density of gas and dust (e.g. Bell et al. 2007; Bayet et al. 2012, in prep.).

Recently, large efforts have been devoted to measuring the CO emission in high-redshift galaxies. These observations have mainly been carried out for higher CO rotational transitions (e.g. Tacconi et al. 2010; Riechers 2011; Genzel et al. 2010; Daddi et al. 2010; Geach et al. 2011). Thus, in order to estimate molecular gas masses from these observations, a connection to the CO(1 – 0) luminosity is needed, as expressed through the CO($J \rightarrow J - 1$)/CO(1 – 0) luminosity ratio. The latter depends upon the excitation of the CO lines and the conditions in the ISM, and is therefore uncertain. The study of several CO transitions, as well as other molecular species, has revealed a wide range of ISM properties that drive large differences in the excitation levels of CO lines in different galaxy types. Through comparisons with PDR and LVG models, a broad distinction has been made between the ISM in normal star-forming galaxies, in starburst-like galaxies, and most recently, the ISM excited by radiation from active galactic nuclei (AGN), suggesting large differences in gas temperature (e.g. Wolfire et al. 2003; Meijerink et al. 2007; van der Werf et al. 2010; Wolfire et al. 2010; van der Werf et al. 2011; Bayet et al. 2011). Ivison et al. (2011) show that large uncertainties are introduced in the study of the CO-to-IR luminosity ratio of galaxies when including measurements which rely on an assumed CO($J \rightarrow J - 1$)/CO(1 – 0) luminosity ratio.

In recent years, efforts have also been made to develop a theoretical framework in a cosmological context to understand the relation between cold, dense gas, SF and other galaxy properties (e.g. Pelupessy et al. 2006; Gnedin et al. 2009; Narayanan et al. 2009, 2012; Bournaud et al. 2010). In particular, a new generation of semi-analytical models of galaxy formation have implemented improved recipes for SF which use more physical descriptions of the ISM of galaxies (Dutton et al. 2010; Fu et al. 2010; Cook et al. 2010; Lagos et al. 2011b). This has allowed a major step forward in the understanding of a wide range of galaxy properties, including

gas and stellar contents and their scaling relations (e.g. Lagos et al. 2011a; Kauffmann et al. 2012). Lagos et al. (2011a) presented simple predictions for CO emission, based on assuming a constant conversion factor between CO luminosity and H_2 mass, and successfully recovered the $L_{CO(1-0)}/L_{IR}$ ratio in normal and starburst galaxies from $z = 0$ to $z = 6$.

Despite this progress, a crucial step in the comparison between observations and theoretical predictions is missing: a physically motivated CO- H_2 conversion factor, X_{CO} . Hydrodynamical cosmological simulations have successfully included the formation of CO, as well as H_2 (e.g. Pelupessy & Papadopoulos 2009), but their high-computational cost does not allow a large number of galaxies spanning a wide range of properties to be simulated to assess the origin of statistical relations such as that between the CO and IR luminosities. Obreschkow et al. (2009) presented a simple phenomenological model to calculate the luminosities of different CO transitions, based on a calculation of the ISM temperature depending on the surface density of SFR and the AGN bolometric luminosity, under the assumption of local thermodynamic equilibrium. However, this modelling introduces several extra free parameters which, in most cases, are not well constrained by observations.

In this paper we propose a theoretical framework to statistically study the connection between CO emission, SF and H_2 mass based on a novel approach which combines a state-of-the-art semi-analytic model of galaxy formation with a single gas phase PDR model of the ISM which outputs the chemistry of the cold ISM. From this hybrid model we estimate the CO emission in different transitions using the predicted molecular content, gas metallicity, UV and X-ray radiation fields in the ISM of galaxies, attempting to include as much of the physics determining X_{CO} as possible. The underlying assumption is that all molecular gas is locked up in GMCs. Although inferences from observations indicate that galaxies have some diffuse H_2 in the outer parts of GMCs that is not traced by the CO emission (e.g. Reach et al. 1994; Grenier et al. 2005), it has been suggested theoretically that this gas represents a constant correction of ≈ 0.3 over a large range of media conditions (Wolfire et al. 2010). We therefore do not attempt to model this diffuse component in this paper and focus on the inner part of the PDRs exclusively, where there is CO emission.

We show in this paper that by coupling a PDR model with the predictions of a galaxy formation model, we are able to explain the observed CO luminosity in several CO transitions and its dependence on IR luminosity. The theoretical framework presented in this paper will help the interpretation of CO observations with the current and next generation of millimeter telescopes, such as the Atacama Large Millimeter Array¹ (ALMA), the Large Millimeter Telescope² (LMT) and the new configuration of the Plateau de Bure Interferometer³ (PdBI). These instruments will produce an unprecedented amount of data, helping to statistically assess the cold gas components of the ISM in both local and high-redshift galaxies.

This paper is organised as follows. In §2 we present the galaxy formation and the PDR models used and describe how we couple the two codes to predict the CO emission in galaxies. §3 presents the predicted CO(1 – 0) emission of galaxies in the local universe, and its relation to other galaxy properties, and compares with available observations. §4 is devoted to the study of the emission of multiple CO lines in the local and high-redshift universe, i.e. the CO

¹ <http://www.almaobservatory.org/>

² <http://www.lmtgtm.org/>

³ <http://www.iram-institute.org/EN>

spectral line energy distribution (SLED), how the CO emission relates to the IR luminosity and how this depends on selected physical ingredients used in the model. In §5 we analyse the assumptions of the PDR model and how these affect the predictions for the CO luminosity. In §6, we focus on the ALMA science case for measuring the cold gas content of high-redshift star-forming galaxies to illustrate the predictive power of the model. We discuss our results and present our conclusions in §6. In Appendix A, we describe how we convert the CO luminosity to the different units used in this paper and how we estimate it from the H_2 mass and X_{CO} .

2 MODELLING THE CO EMISSION OF GALAXIES

We study the CO emission from the $(1-0)$ to the $(10-9)$ rotational transitions, and its relation to other galaxy properties, using a modified version of the GALFORM semi-analytical model of galaxy formation described by Lagos et al. (2011a, 2011b) in combination with the Photon Dominated Region code, UCL-PDR of Bayet et al. (2011). In this section we describe the galaxy formation model and the physical processes included in it in §2.1, the UCL-PDR model and its main parameters in §2.2, give details about how we couple these two models to estimate the CO emission of galaxies in §2.3, and briefly describe how the CO conversion factor depends on galaxy properties predicted by GALFORM in §2.4.

2.1 The galaxy formation model

The GALFORM model (Cole et al. 2000) takes into account the main physical processes that shape the formation and evolution of galaxies. These are: (i) the collapse and merging of dark matter (DM) halos, (ii) the shock-heating and radiative cooling of gas inside DM halos, leading to the formation of galactic disks, (iii) quiescent star formation (SF) in galaxy disks, (iv) feedback from supernovae (SNe), from AGN and from photo-ionization of the intergalactic medium (IGM), (v) chemical enrichment of stars and gas, and (vi) galaxy mergers driven by dynamical friction within common DM halos, which can trigger bursts of SF and lead to the formation of spheroids (for a review of these ingredients see Baugh 2006; Benson 2010). Galaxy luminosities are computed from the predicted star formation and chemical enrichment histories using a stellar population synthesis model. Dust extinction at different wavelengths is calculated self-consistently from the gas and metal contents of each galaxy and the predicted scale lengths of the disk and bulge components using a radiative transfer model (see Cole et al. 2000 and Lacey et al. 2011). Lagos et al. (2011b) improved the treatment of SF in quiescent disks, (iii) in the above list, which allowed more general SF laws to be used in the model.

GALFORM uses the formation histories of DM halos as a starting point to model galaxy formation (see Cole et al. 2000). In this paper we use halo merger trees extracted from the Millennium N-body simulation (Springel et al. 2005), which assumes the following cosmological parameters: $\Omega_m = \Omega_{DM} + \Omega_{baryons} = 0.25$ (with a baryon fraction of 0.18), $\Omega_\Lambda = 0.75$, $\sigma_8 = 0.9$ and $h = 0.73$. The resolution of the N-body simulation corresponds to a minimum halo mass of $1.72 \times 10^{10} h^{-1} M_\odot$. This is sufficient to resolve the halos that contain most of the H_2 in the universe at $z < 8$ (Lagos et al. 2011a).

Lagos et al. (2011b) studied three SF laws, (i) the empirical SF law of Kennicutt (1998), (ii) the empirical SF law of Blitz & Rosolowsky (2006) and (iii) the theoretical SF law of Krumholz et al. (2009b). Here we follow Lagos et al.

(2011a, hereafter L11), who adopted the empirical SF law of Blitz & Rosolowsky (2006) as their preferred model. The main successes of the L11 model include the reproduction of the optical and near-infrared luminosity functions (LF), the $z = 0$ atomic hydrogen (HI) mass function (MF), the global density evolution of HI at $z < 3.5$, and scaling relations between HI, H_2 , stellar mass and galaxy morphology in the local Universe.

The Blitz & Rosolowsky (2006) empirical SF law has the form

$$\Sigma_{SFR} = \nu_{SF} f_{mol} \Sigma_{gas}, \quad (1)$$

where Σ_{SFR} and Σ_{gas} are the surface densities of SFR and the total cold gas mass, respectively, ν_{SF} is the inverse of the SF timescale for the molecular gas and $f_{mol} = \Sigma_{mol}/\Sigma_{gas}$ is the molecular to total gas mass surface density ratio. The molecular and total gas contents include the contribution from helium, while HI and H_2 masses only include hydrogen (helium accounts for 26% of the overall cold gas mass). The ratio f_{mol} is assumed to depend on the internal hydrostatic pressure of the disk as $\Sigma_{H_2}/\Sigma_{HI} = f_{mol}/(f_{mol} - 1) = (P_{ext}/P_0)^\alpha$ (Blitz & Rosolowsky 2006). The parameters values we use for ν_{SF} , P_0 and α are the best fits to observations of spirals and dwarf galaxies, $\nu_{SF} = 0.5 \text{ Gyr}^{-1}$, $\alpha = 0.92$ and $\log(P_0/k_B[\text{cm}^{-3}\text{K}]) = 4.54$ (Blitz & Rosolowsky 2006; Leroy et al. 2008; Bigiel et al. 2011; Rahman et al. 2012). Mac Low & Glover (2012) explain the relation between the Σ_{H_2}/Σ_{HI} ratio and the midplane pressure being the result of an underlying and more fundamental relation between these two quantities and the local density in normal spiral galaxies (see also Pelupessy & Papadopoulos 2009). In this paper, however, we adopt the empirical relation to avoid fine-tuning of the parameters associated with it (see Lagos et al. 2011b).

For starbursts the situation is less clear. Observational uncertainties, such as the conversion factor between CO and H_2 in starbursts, and the intrinsic compactness of star-forming regions, have not allowed a clear characterisation of the SF law (e.g. Kennicutt 1998; Genzel et al. 2010; Combes et al. 2011). Theoretically, it has been suggested that the SF law in starbursts is different from that in normal star-forming galaxies: the relation between Σ_{H_2}/Σ_{HI} and gas pressure is expected to be different in environments of very high gas densities typical of starbursts (Pelupessy et al. 2006; Pelupessy & Papadopoulos 2009; Mac Low & Glover 2012), where the ISM is predicted to always be dominated by H_2 independently of the exact gas pressure. For these reasons we choose to apply the Blitz & Rosolowsky SF law only during quiescent SF (fuelled by the accretion of cooled gas onto galactic disks) and retain the original SF prescription for starbursts (see Cole et al. 2000 and L11 for details). In the latter, the SF timescale is taken to be proportional to the bulge dynamical timescale above a minimum floor value (which is a model parameter) and involves the whole ISM gas content in the starburst, giving $SFR = M_{gas}/\tau_{SF}$ (see Granato et al. 2000 and Lacey et al. 2008 for details), with

$$\tau_{SF} = \max(\tau_{min}, f_{dyn} \tau_{dyn}). \quad (2)$$

Here we adopt $\tau_{min} = 100 \text{ Myr}$ and $f_{dyn} = 50$. This parameter choice helps to reproduce the observed rest-frame UV (1500\AA) luminosity function from $z \approx 3$ to $z \approx 6$ (see Baugh et al. 2005; Lacey et al. 2011). In Lagos et al. (2011a) these parameters were set to $\tau_{min} = 5 \text{ Myr}$ and $f_{dyn} = 2$, inherited from the parameter choice in Bower et al. (2006). However, the modification of these two parameters does not have any relevant influence on the results presented previously in Lagos et al. (2011a,b), but mainly affects

the UV luminosity of very high redshift galaxies through the dust production during starbursts.

In order to estimate the CO emission in starbursts, we assume here that the cold gas content is fully molecular, $f_{\text{mol}} = 1$. Note that this is similar to assuming that the Blitz & Rosolowsky relation between the midplane pressure and the $\Sigma_{\text{H}_2}/\Sigma_{\text{HI}}$ ratio holds in starbursts, given that large gas and stellar densities lead to $f_{\text{mol}} \approx 1$. Throughout the paper we will refer to galaxies as ‘starburst galaxies’ if their total SFR is dominated by the starburst mode, $\text{SFR}_{\text{starburst}} > \text{SFR}_{\text{quiescent}}$, while the rest of the galaxies will be referred to as ‘quiescent galaxies’.

2.1.1 Estimating the properties of the interstellar medium of galaxies in GALFORM

The three properties predicted by GALFORM which we use as inputs for the PDR model are (1) the ISM metallicity, Z_{gas} , (2) the average internal FUV radiation field, G_{UV} , and (3) the average internal hard X-ray radiation field, F_{X} . In this subsection we describe how these three properties are estimated and compare with observations in the case of Z_{gas} .

- Z_{gas} . In GALFORM, Z_{gas} corresponds to the total mass fraction in metals in the ISM, and is calculated by assuming instantaneous recycling. Z_{gas} is the result of the non-linear interplay between the existing metal content in the ISM, the metal content of the incoming cooled gas, which originated in the hot halo, and the metals ejected by dying stars (Cole et al. 2000).

The top-panel of Fig. 1 shows the gas metallicity as a function of the B -band luminosity for galaxies in the model compared to the observational results of Contini et al. (2002), Melbourne & Salzer (2002), Lamareille et al. (2004) and Tremonti et al. (2004). A correction factor needs to be applied to the observations to convert from the inferred abundance of oxygen relative to hydrogen, O/H , to Z_{gas} . We use the solar metallicity ratios reported by Asplund et al. (2005), $\text{O}/\text{H}_{\odot} = 4.57 \times 10^{-4}$ and $Z_{\odot} = 0.0122$. This choice of the value of solar abundance is to keep consistency with the solar abundance assumed in the UCL-PDR model. In the case of the Tremonti et al. (2004) data, we applied the conversion suggested by these authors to derive a B -band luminosity-metallicity relation from their g -band relation. The luminosity-metallicity relations estimated by Tremonti et al. (2004) and Lamareille et al. (2004) used large area redshift surveys (the Sloan Digital Sky Survey and the 2 Degree Field Galaxy Redshift survey, respectively). In the case of Contini et al. (2002) and Melbourne & Salzer (2002), results were based on smaller samples of star-forming galaxies which were followed up in spectroscopy. The Contini et al. (2002) B -band luminosity-metallicity relation was derived from a sample of UV-selected galaxies, which includes a few higher redshift galaxies with $z > 0.15$.

The observational results shown in Fig. 1 use abundance indicators based on emission lines to calculate oxygen abundances. To estimate oxygen abundances, Contini et al. (2002), Melbourne & Salzer (2002) and Lamareille et al. (2004) use an empirical relation between oxygen abundance and the R_{23} abundance ratio, where $R_{23} = ([\text{OII}] + [\text{OIII}])/\text{H}\beta$, which is often called the ‘strong-line’ technique. Tremonti et al. (2004), on the other hand, fit all prominent emission lines with a model designed to describe integrated galaxy spectra, which includes HII regions and diffuse ionized gas. Kennicutt et al. (2003) compared the ‘strong-line’ technique with abundances inferred from electron temperature measurements in a sample of HII regions with very high resolution

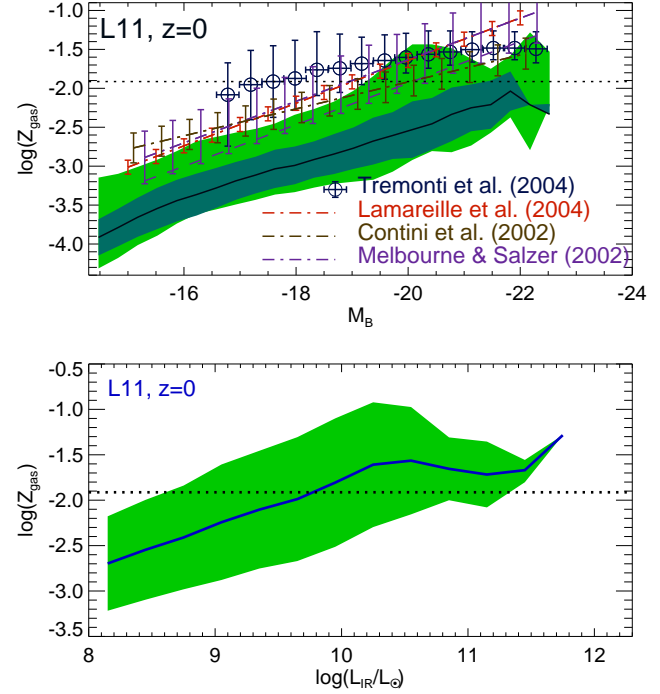


Figure 1. *Top-panel:* Gas metallicity vs. dust extincted B -band absolute magnitude of galaxies at $z = 0$ in the L11 model. The solid line and the dark shaded area show the median and the 10 to 90 percentile range of model galaxies in the L11 model with an equivalent width of the $\text{H}\beta$ line $\text{EW}(\text{H}\beta) > 1.5\text{\AA}$. The lighter colour shaded region shows the 10 to 90 percentile range of all model galaxies with $\text{SFR} > 0$. The best fit and standard deviation of the observed gas metallicity-luminosity relations are shown as dot-dashed lines with errorbars (Lamareille et al. 2004; Contini et al. 2002; Melbourne & Salzer 2002). Circles and errorbars show the median and 2σ range on the observational estimates of Tremonti et al. (2004), using their correction to convert the g -band luminosity-metallicity relation to the B -band. Note that the observational data correspond to a metallicity inferred from emission lines coming from the central parts of galaxies (i.e. emission within the fiber, which is of a diameter 2 arcsec in the case of 2dFGRS in Lamareille et al. 2004, 3 arcsec in the case of SDSS in Tremonti et al. 2004, and 2 and 3.5 arcsecs in the smaller surveys of Contini et al. 2002 and Melbourne & Salzer 2002, respectively). We also show the Melbourne & Salzer (2002) median relation shifted by -0.3 dex (dashed line) to illustrate the possible systematic error in the strong line method (see text for details). *Bottom-panel:* Gas metallicity vs. IR luminosity for the L11 model. Here we include all model galaxies. For reference, the solar metallicity value reported by Asplund et al. (2005) is shown as a horizontal dotted line in both panels.

spectroscopy, and argued that the empirical ‘strong-line’ method systematically results in larger abundances by approximately a factor of 2 due to uncertainties in the nebular models used in calibration. In order to illustrate this possible systematic error, we show as a dashed line the relation of Melbourne & Salzer (2002) data shifted by -0.3 dex.

The L11 model predicts a lower normalization of the luminosity-metallicity relation than implied by observations, but with a similar slope. When selecting star-forming galaxies in the model by their $\text{H}\beta$ equivalent width, this discrepancy increases due to the tighter gas metallicity-luminosity relation predicted for these galaxies. The correction suggested by Kennicutt et al. (2003) to remove the systematic introduced by the ‘strong-line’ technique reduces the dis-

crepancy between the observed and predicted median relations to a factor 2, well within the typical dispersion of observational data (see errorbars for Tremonti et al. 2004 in Fig. 1). Another caveat in the comparison between observations and the model predictions is the fact that the observational data are inferred from the emission lying within a spectrograph fiber (typically of 3 arcsecs or less in diameter), which typically covers only the central parts of the galaxy, and therefore are not global mass-weighted metallicities. Galaxies show metallicity gradients, with the central parts being more metal rich than the outskirts (e.g. Peletier et al. 1990; de Jong 1996). The differences in metallicity between centers and the outer regions of galaxies can be as large as a factor 2 – 3 in early-type galaxies and 3 – 10 in late-type galaxies (Henry & Worthey 1999). Thus, one would expect metallicities inferred from the fibers to be upper limits for the mass-weighted ISM metallicity. Given this caveat, the model predictions are in reasonable agreement with the observations.

Throughout the paper we make extensive comparisons between the CO and total IR luminosity (see Appendix A for a description of how we calculate the IR luminosity in GALFORM). We plot in the bottom-panel of Fig. 1, the gas metallicity as a function of the IR luminosity. For $L_{\text{IR}} < 10^{10} L_{\odot}$, the gas metallicity increases with L_{IR} , but tends to a constant value at higher luminosities. As we show later in the text, the dependence of the CO emission on IR luminosity is influenced by the gas metallicity (§3 and §4), as it alters both luminosities. The bottom panel of Fig. 1 will therefore help in the interpretation of the results later in this paper.

- G_{UV} . The average internal UV radiation field, G_{UV} , corresponds to a local radiation field that depends on the transmission of UV photons from star-forming regions and their propagation through the diffuse ISM. The exact transmitted fraction of UV radiation depends on the local conditions in the ISM, such as the optical depth, the ratio of gas in the diffuse ISM and in GMCs, etc (see Lacey et al. 2011). Whilst G_{UV} is a local property, we make a rough estimate by considering two simple approximations which are based on global galaxy properties. The first scaling is motivated by the close relation between UV luminosity and SFR (Lacey et al. 2011), so that in an optically thin slab, the average UV flux scales approximately as $\langle I_{\text{UV}} \rangle \propto \Sigma_{\text{UV}} \propto \Sigma_{\text{SFR}}$. This is expected if the UV radiation field in the wavelength range considered here ($\lambda = 900 - 2100 \text{ \AA}$) is dominated by radiation from OB stars. We therefore assume that G_{UV} is related to the surface density of SFR by

$$\frac{G_{\text{UV}}}{G_0} = \left(\frac{\Sigma_{\text{SFR}}}{\Sigma_{\text{SFR}}^0} \right)^{\gamma}. \quad (3)$$

Here we take $\Sigma_{\text{SFR}} = \text{SFR}/2\pi r_{50}^2$, where r_{50} corresponds to the half-mass radius, either of the disk or the bulge, depending on where the SF is taking place (in the disk for quiescent SF and in the bulge for starbursts). We set $\gamma = 1$ so that G_{UV} increases by the same factor as Σ_{SFR} . However, values of $\gamma = 0.5 - 2$ do not change the predictions of the model significantly. For the normalisation, we choose $\Sigma_{\text{SFR}}^0 = 10^{-3} M_{\odot} \text{ yr}^{-1} \text{ kpc}^{-2}$, so that $G_{\text{UV}} = G_0 = 1.6 \times 10^{-3} \text{ erg cm}^{-2} \text{ s}^{-1}$ for the solar neighborhood (Bonatto & Bica 2011).

A dependence of G_{UV} solely on Σ_{SFR} assumes that an increase in the local UV radiation field takes place if a galaxy forms stars at a higher rate per unit area, but does not take into account the transparency of the gas. To attempt to account for this, we consider an alternative scaling in which we include in a simple way the average optical depth of the ISM in the description of G_{UV} . In a slab, the transmission probability of UV photons, β_{UV} , scales with the

optical depth, τ_{UV} , so that $\beta_{\text{UV}} \sim (1 - e^{-\tau_{\text{UV}}})/\tau_{\text{UV}}$. The optical depth, on the other hand, depends on the gas metallicity and column density of atoms as $\tau_{\text{UV}} \propto Z_{\text{gas}} N_{\text{H}}$. In optically thick gas ($\tau_{\text{UV}} \gg 1$), $\beta_{\text{UV}} \sim \tau_{\text{UV}}^{-1}$. By assuming that the average local UV field depends on the average emitted UV field ($\langle I_{\text{UV}} \rangle \propto \Sigma_{\text{SFR}}$) times an average UV transmission factor, we get the scaling

$$\frac{G_{\text{UV}}}{G_0} = \left(\frac{\Sigma_{\text{SFR}}/\Sigma_{\text{SFR}}^0}{[Z_{\text{gas}}/Z_{\odot}][\Sigma_{\text{gas}}/\Sigma_{\text{gas}}^0]} \right)^{\gamma'}. \quad (4)$$

We set $\gamma' = 1$, but as with Eq. 3, varying the exponent in the range $\gamma' = 0.5 - 2$ has little impact on the model predictions (see §4). We use the solar neighborhood value, $\Sigma_{\text{gas}}^0 = 10 M_{\odot} \text{ pc}^{-2}$ (Chang et al. 2002). The parametrization of Eq. 4 has been shown to explain the higher G_{UV} in the Small Magellanic Cloud compared to the Milky-Way, which is needed to explain the low molecular-to-atomic hydrogen ratios (Bolatto et al. 2011). We test these two parametrizations of G_{UV} against broader observations in §3 and §4.

- F_{X} . In GALFORM we model the growth and emission by supermassive black holes (SMBHs) which drive AGN in galaxies (Fanidakis et al. 2011). Fanidakis et al. (2012) estimate the emission from accreting SMBHs over a wide wavelength range, from hard X-rays to radio wavelengths. The SMBH modelling of Fanidakis et al. includes an estimate of the efficiency of energy production by accretion onto the black hole, taking into account the value of the black hole spin, which is followed through all the gas accretion episodes and mergers with other black holes. Fanidakis et al. (2012) show that the model can successfully explain the LF of AGN and quasars and its time evolution at different wavelengths. In this work we use this SMBH modelling to take into account the heating of the ISM by the presence of an AGN in the galaxy, which has been shown to be important in the hard X-ray energy window (Meijerink et al. 2007). The emission of AGN in hard X-rays (2 – 10 KeV), L_{X} , is calculated in Fanidakis et al. using the bolometric luminosity of the AGN and the bolometric corrections presented in Marconi et al. (2004). We estimate the average hard X-ray flux, F_{X} , at the half-mass radius of the bulge,

$$F_{\text{X}} = \frac{L_{\text{X}}}{4\pi r_{50}^2}. \quad (5)$$

2.2 The UCL-PDR code

The UCL-PDR code attempts to fully describe the chemical and thermal evolution of molecular clouds under different conditions in the surrounding ISM as quantified by: the far-UV (FUV) radiation background, the cosmic ray background, the volume number density of hydrogen, the average dust optical depth and the gas metallicity (see Bell et al. 2006; 2007 for a detailed description). More recently, Bayet et al. (2009a) and Bayet et al. (2011) explored these parameters for the ISM in external galaxies. We use the code released by Bayet et al. (2011), in which additional cooling mechanisms were included, such as $^{13}\text{C}^{16}\text{O}$, $^{12}\text{C}^{18}\text{O}$, CS and OH. Bayet et al. (2011) showed that these coolants are important when dealing with galaxies which are forming stars at high rates.

The UCL-PDR code is a time-dependent model which treats a cloud as a one-dimensional, semi-infinite slab illuminated from one side by FUV photons. Molecular gas described by the PDR code correspond to clouds having a single gas phase, with a single gas volume density, although gradients in temperature and chemical composition depend on the optical depth. The radiative transfer equations are solved and the thermal balance between heating

and cooling mechanisms is calculated leading to the determination of the gradients of kinetic temperature, chemical composition and emission line strength across the slab (i.e. as a function of optical extinction in the visible, A_V). The gas kinetic temperature at which this balance is achieved will be referred to throughout the paper as the typical kinetic temperature of molecular clouds in galaxies in the model, T_K .

The starting point in the model is to assume that hydrogen is mostly molecular and that other species are atomic. The model follows the relative abundance of 131 species, including atoms and molecules, using a network of more than 1,700 chemical reactions (see Bayet et al. 2009b; Bayet et al. 2011). The initial element abundances, dust-to-gas ratio and H_2 formation rate are assumed to scale linearly with the metallicity of the gas.

The physical mechanisms included in the UCL-PDR code are (i) H_2 formation on dust grain surfaces, (ii) H_2 photodissociation by FUV radiation (which we define as the integrated emission for the wavelength range $\lambda = 900 - 2100 \text{ \AA}$), (iii) H_2 UV fluorescence, (iv) the photoelectric effect from silicate grains and polycyclic aromatic hydrocarbons (PAHs), (v) C II recombination and (vi) interaction of low-energy cosmic-rays (CRs) with the gas, which boosts the temperature of the gas. The latter results in stronger CO emission from high order rotational transitions that resembles the observed CO emission from galaxies which host AGN. The CO spectral line energy distribution (commonly referred to as the CO ladder or SLED) therefore can be obtained for a wide range of parameters included in the UCL-PDR code.

Given that the ISM of galaxies is not resolved in GALFORM, we assume the following fiducial properties for GMCs. We adopted a gas density of $n_H = 10^4 \text{ cm}^{-3}$, where each model was run for 10^6 yr . Note that n_H represents the total number of hydrogen nuclei. The value of n_H adopted is similar to the assumption used previously in GALFORM for GMCs (i.e. $n_H = 7 \times 10^3 \text{ cm}^{-3}$; Granato et al. 2000; Lacey et al. 2011), which in turn is motivated by the assumptions used in the GRASIL code (Silva et al. 1998), which calculates the reprocessing of stellar radiation by dust. The parameters above correspond to star-forming gas which is likely to be opaque to radiation. Note that this dense gas phase typically has A_V in the range 3 – 8 mag. We choose to focus on dense gas of $A_V = 8 \text{ mag}$ to obtain a $X_{CO(1-0)}$ for the local neighbourhood properties consistent with observational results. We expect this approximation to be accurate particularly in gas-rich galaxies, which to first order have a larger proportion of gas in this dense phase with respect to the total gas reservoir compared to more passive galaxies. This is simply because of the energetics and the dynamics involved in highly star-forming regions, which typically increase both density and temperature, leading to a more dense, opaque and fragmented medium (see Bayet 2008, 2009 for more details). Note, however, that the assumption of a lower A_V for lower gas surface density galaxies, $\Sigma_{\text{gas}} < 10^7 M_\odot \text{ kpc}^{-2}$, would not affect the results shown in this paper, for example simply moving galaxies along the fainter part of the CO luminosity function, without modifying its bright-end.

Wolfire et al. (2003) suggested that a minimum density $n_{H,\text{min}} \propto G_{UV}$ is necessary to obtain pressure balance between the warm and cold neutral media in the ISM. All the models shown in Table 1 fulfill this condition, with $n_H > n_{H,\text{min}}$. However, we test the effect of assuming that n_H scales with the minimum density of Wolfire et al. (2003), which leads to $n_H \propto G_{UV}$. With this in mind, we ran four more models with n_H varying in such a way that the n_H/G_{UV} ratio is left invariant, in addition to the PDR models run

using $n_H = 10^4 \text{ cm}^{-3}$. We analyse the CO luminosities predicted by this set of models in §5.

The output of the UCL-PDR code includes the conversion factor, $X_{CO(J \rightarrow J-1)}$, between the intensity of a particular CO rotational transition and the column number density of H_2 molecules,

$$X_{CO(J \rightarrow J-1)} = \frac{N_{H_2}}{I_{CO(J \rightarrow J-1)}}, \quad (6)$$

where N_{H_2} is the H_2 column density and I_{CO} is the integrated CO line intensity (see Appendix A). This conversion factor, which is the one we are interested in here, depends on the conditions in the ISM.

We present, for the first time, the conversion factors for different transitions predicted by the UCL-PDR model. The output is listed in Table 1 for 41 different combinations of input properties of the ISM, where 37 models use $n_H = 10^4 \text{ cm}^{-3}$, and 4 have variable n_H , chosen so that n_H/G_{UV} is constant. These values are intended to span the range of possibilities in the galaxy population as a whole, ranging from low metallicity dwarf galaxies to metal rich starbursts. These models consider UV radiation field strengths of 1, 10, 100 and 1000 times the value in our local neighbourhood ($G_0 = 1.6 \times 10^{-3} \text{ erg cm}^{-2} \text{ s}^{-1}$), gas metallicities ranging from $Z_{\text{gas}} = 0.01 - 2 Z_\odot$ and a flux (in the hard X-rays window) of 0.01, 0.1 and $1 \text{ erg s}^{-1} \text{ cm}^{-2}$ (where X-rays are used as a proxy for cosmic rays; see Papadopoulos 2010; Meijerink et al. 2011; Bayet et al. 2011). The UCL-PDR model inputs the cosmic rays ionization rate instead of hard X-rays flux. We assume a direct proportionality between the cosmic ray ionization rate and hard X-rays flux following the studies of Meijerink et al. (2011) and Bayet et al. (2011), where $F_X/F_0 = \zeta_{CR}/\zeta_0$, with $F_0 = 0.01 \text{ erg s}^{-1} \text{ cm}^{-2}$ and $\zeta_0 = 5 \times 10^{-17} \text{ s}^{-1}$. We only list the CO- H_2 conversion parameters of three CO transitions in Table 1. However, the UCL-PDR model was run to output all CO transitions from 1 – 0 to 10 – 9, which we use to construct CO SLEDs in §4 and §6. A comprehensive analysis and results of the PDR model listed in Table 1 will be presented in Bayet et al. (2012, in prep.).

From Table 1 it is possible to see that the general dependence of X_{CO} on the three properties Z_{gas} , G_{UV} and F_X , depends on the transition considered. For instance, $X_{CO(1-0)}$ increases as the gas metallicity decreases, but its dependence on G_{UV} and F_X depends on the gas metallicity: for solar or supersolar metallicities, $X_{CO(1-0)}$ tends to decrease with increasing G_{UV} and F_X , given that the higher temperatures increase the CO(1 – 0) emission. However, for very subsolar gas metallicities, these trends are the opposite: $X_{CO(1-0)}$ tends to increase with increasing G_{UV} and F_X . In this case this is due to the effect of the high radiation fields and the lack of an effective CO self-shielding, which destroys CO molecules. In the case of higher CO transitions, for example CO(7 – 6), $X_{CO(7-6)}$ generally increases with decreasing kinetic temperature, however this is not strictly the case in every set of parameters. These general trends will help explain the relations presented in §3 – 4 and §6.

At very low metallicities, $Z_g \approx 0.01 Z_\odot$, the CO lines become optically thin in some of the cases, e.g. in those models where there is a high UV and X-ray flux illuminating the molecular clouds. This represents a limitation of the PDR model given the uncertainties in the opacity effect on the CO lines. However, such galaxies are extremely rare in our model after selecting galaxies with $L_{IR} > 10^9 L_\odot$, which are those we use to study the CO SLED at redshifts $z > 0$ (e.g. only 0.05% of galaxies with $L_{IR} > 10^9 L_\odot$ at $z = 6$ have $Z_g \leq 0.01 Z_\odot$). This is not the case for very faint IR galaxies.

Table 1. Conversion factors from CO(1 – 0)-H₂ (6), CO(3 – 2)-H₂ (7) and CO(7 – 6)-H₂ (8) in units of $10^{20} \text{ cm}^{-2} (\text{K km s}^{-1})^{-1}$, and the kinetic temperature of the gas (9) for galaxies with different ISM conditions: (1) FUV radiation background, G_{UV} , in units of $G_0 = 1.6 \times 10^{-3} \text{ erg cm}^{-2} \text{ s}^{-1}$, (2) gas metallicity, Z_{gas} , in units of $Z_{\odot} = 0.0122$, (3) hard X-ray flux, F_{X} , in units of $\text{erg s}^{-1} \text{ cm}^{-2}$ and (4) total number of hydrogen nuclei, n_{H} , in units of cm^{-3} (Bell et al. 2006; Asplund et al. 2005).

(1)	(2)	(3)	(4)	(5)	(6)	(7)	(8)	(9)
G_{UV}/G_0	Z_{gas}/Z_{\odot}	$F_{\text{X}}/\text{erg s}^{-1} \text{ cm}^{-2}$	$n_{\text{H}}/\text{cm}^{-3}$	$(n_{\text{H}}/\text{cm}^{-3})/(G_{\text{UV}}/G_0)$	$X_{\text{CO}(1-0)}$	$X_{\text{CO}(3-2)}$	$X_{\text{CO}(7-6)}$	T_{K}/K
1	0.01	0.01	10^4	10^4	3.585	2.335	24.091	39.37
1	0.05	0.01	10^4	10^4	3.212	4.007	100.043	17.95
1	0.1	0.01	10^4	10^4	3.177	4.168	218.343	19.44
1	0.5	0.01	10^4	10^4	2.760	4.105	1281.91	12.33
1	1	0.01	10^4	10^4	1.883	2.808	1124.70	10.47
1	2	0.01	10^4	10^4	1.015	1.521	747.670	8.72
1	0.01	0.1	10^4	10^4	3.620	1.817	9.311	51.24
1	0.1	0.1	10^4	10^4	3.293	3.072	55.812	38.61
1	1	0.1	10^4	10^4	1.519	2.103	96.234	19.26
1	2	0.1	10^4	10^4	0.915	1.283	111.9	15.69
1	0.01	1	10^4	10^4	6.260	3.688	63.556	107.78
1	0.1	1	10^4	10^4	2.389	1.653	5.509	60.81
1	1	1	10^4	10^4	2.263	1.853	56.680	38.82
1	2	1	10^4	10^4	0.999	0.956	20.411	38.33
10	0.01	0.01	10^4	10^3	3.856	2.393	27.359	38.93
10	0.1	0.01	10^4	10^3	2.970	3.274	193.999	18.73
10	1	0.01	10^4	10^3	1.139	1.392	48.991	10.22
10	2	0.01	10^4	10^3	0.596	0.726	24.525	8.64
10	0.01	1	10^4	10^3	6.468	3.759	66.494	104.35
10	0.1	1	10^4	10^3	2.382	1.627	5.510	60.72
10	1	1	10^4	10^3	2.003	1.518	35.534	39.13
100	0.01	0.01	10^4	10^2	3.673	3.513	190.302	38.17
100	0.1	0.01	10^4	10^2	3.174	3.441	225.733	18.00
100	1	0.01	10^4	10^2	0.913	1.005	12.726	9.63
100	0.01	1.0	10^4	10^2	13.73	2.477	5.428	98.49
100	0.1	1.0	10^4	10^2	2.237	1.839	10.591	60.57
100	1	1.0	10^4	10^2	1.861	1.312	24.277	38.94
1000	0.01	0.01	10^4	10	4.560	4.061	295.512	39.35
1000	0.1	0.01	10^4	10	3.059	3.237	195.177	16.33
1000	1	0.01	10^4	10	0.809	0.867	6.771	8.78
1000	2	0.01	10^4	10	0.374	0.385	2.094	7.86
1000	0.01	0.1	10^4	10	2.592	3.841	102.544	19.58
1000	0.1	0.1	10^4	10	2.149	3.146	103.455	19.51
1000	1	0.1	10^4	10	1.519	2.103	96.234	19.26
1000	0.01	1.0	10^4	10	15.475	2.664	5.859	113.55
1000	0.1	1.0	10^4	10	2.722	1.536	6.020	59.83
1000	1	1.0	10^4	10	2.263	1.853	56.680	38.82
1	1	0.01	10^3	10^3	2.692	7.374	6.3×10^4	11.49
100	1	0.01	10^5	10^3	0.793	0.659	1.52	7.59
1000	1	0.01	10^6	10^3	0.542	0.358	0.421	6.16
1000	1	1	10^6	10^3	0.691	0.43	0.513	21.18

We find that in the subsample of galaxies with $L_{\text{IR}} > 10^7 L_{\odot}$, more than 10% of galaxies have $Z_{\text{g}} \leq 0.01 Z_{\odot}$ at $z > 1.5$.

2.3 Coupling the GALFORM and UCL-PDR codes

We use the properties Z_{gas} , G_{UV} and F_{X} as inputs to the UCL-PDR model. For each galaxy, we calculate the X_{CO} conversion factors for several CO transitions, and use the molecular mass of the galaxy to estimate the CO luminosity of these transitions (see Appendix A). We use the models from Table 1 to find the X_{CO} conversion factors and the gas kinetic temperature of molecular clouds, T_{K} , for each galaxy according to its ISM properties.

Given that Z_{gas} , G_{UV} and F_{X} are discretely sampled, we interpolate over the entries of Table 1 on a logarithmic scale in each parameter. Throughout the paper we will refer to the coupled code as the GALFORM+UCL-PDR model.

Galaxies in GALFORM can have SF taking place simultaneously in the disk and the bulge, corresponding to the quiescent and starburst SF modes, respectively. The gas reservoirs of these two modes are different and we estimate the CO luminosity of the two phases independently. This can be particularly important at high-redshift, where the galaxy merger rate is higher and where galaxies are more prone to have dynamically unstable disks, which can lead to starbursts. For instance, Danielson et al. (2010) showed that two

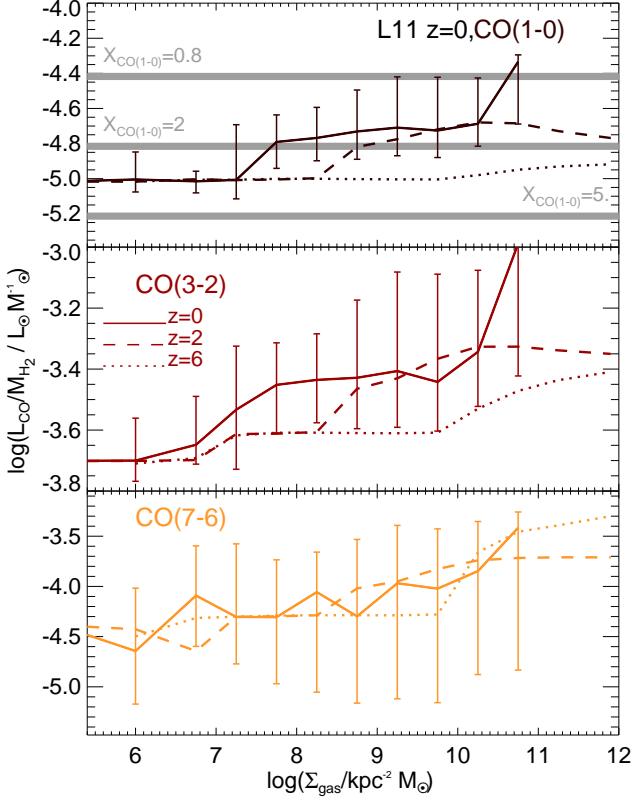


Figure 2. CO luminosity-to-molecular hydrogen mass ratio as a function of the average gas surface density of galaxies in GALFORM at $z = 0$ (solid lines), $z = 2$ (dashed lines) and $z = 6$ (dotted lines) for the CO transitions (1 – 0) (top panel), (3 – 2) (middle panel) and (7 – 6) (bottom panel). Lines show the median of the predicted distributions, and error bars show the 10 and 90 percentiles, which are shown, for clarity, only for one redshift in each panel. For reference, in the top panel, the thick, horizontal lines show the ratios for fixed conversion factors: $X_{\text{CO}(1-0)} = (0.8, 2, 5) \times 10^{20} \text{ cm}^{-2} (\text{K km s}^{-1})^{-1}$, corresponding to the values typically adopted in observational studies for starburst, normal star-forming and dwarf galaxies, respectively.

gas phases, a diffuse and a dense phase, are necessary to describe the CO spectral line energy distribution of the $z = 2.3$ galaxy SMM J2135-0102 (see also Bothwell et al. 2012), illustrating the importance of allowing for the possibility of concurrent quiescent and burst episodes of SF in the modelling of CO emission.

2.4 The dependence of the CO-H₂ conversion factor on galaxy properties in GALFORM

In order to illustrate how much the X_{CO} conversion factor varies with galaxy properties, in this subsection we focus on the predictions of the CO luminosity-to-molecular mass ratio in the GALFORM+UCL-PDR model in the case where G_{UV} depends on Z_{gas} , Σ_{SFR} and Σ_{gas} (see Eq. 4).

Fig. 2 shows the $L_{\text{CO}}/M_{\text{H}_2}$ ratio as a function of the average ISM gas surface density, Σ_{gas} , at three different redshifts, and for three different CO transitions. In the case of CO(1 – 0), we show for reference the standard conversion factors typically adopted in the literature for starburst, normal spiral and dwarf galaxies as horizontal lines. At $z = 0$ there is, on average, a positive correlation

between $L_{\text{CO}}/M_{\text{H}_2}$ and Σ_{gas} , with $L_{\text{CO}}/M_{\text{H}_2} \propto \Sigma_{\text{gas}}^{0.15}$, regardless of the CO transition. At higher redshifts, the relation between the $L_{\text{CO}}/M_{\text{H}_2}$ ratio and Σ_{gas} flattens, mainly due to the lower gas metallicities of galaxies. These trends are similar for all the CO transitions. In the case of the CO(1 – 0) at $z = 0$, galaxies of low Σ_{gas} have X_{CO} closer to the value measured in dwarf galaxies moving to values closer to starburst galaxies at very high Σ_{gas} . In terms of stellar mass, galaxies with $M_{\text{stellar}} \approx 7 \times 10^{10} M_{\odot}$, close to the Milky-Way stellar mass, have on average $X_{\text{CO}(1-0)} \approx 2 - 3 \times 10^{20} \text{ cm}^{-2} (\text{K km s}^{-1})^{-1}$, in agreement with the measurements of the solar neighbourhood. For relatively massive galaxies, the model predicts that the $L_{\text{CO}}/M_{\text{H}_2}$ ratio evolves only weakly with redshift at $z \lesssim 2$, which explains the similarity between the $X_{\text{CO}(1-0)}$ measured by Daddi et al. (2010) in normal star-forming galaxies at $z \approx 1.5$ and the value for local spiral galaxies.

The coupled GALFORM+UCL-PDR model thus predicts a dependence of X_{CO} on galaxy properties which broadly agrees with observations in the local Universe and explains the few observations of high-redshift galaxies.

3 THE CO(1-0) EMISSION OF GALAXIES IN THE LOCAL UNIVERSE

In the local Universe, the CO(1 – 0) emission of galaxies has been studied extensively in different environments with large samples of galaxies (e.g. Keres et al. 2003; Solomon & Vanden Bout 2005; Bothwell et al. 2009; Saintonge et al. 2011; Lisenfeld et al. 2011). In this section we compare our predictions for the CO(1 – 0) emission of galaxies at $z = 0$ and how this relates to their IR luminosity, with available observations.

3.1 The CO(1-0) luminosity function

In this subsection we focus on the CO(1 – 0) LF and how the predictions depend on the assumptions and the physics of the model.

Fig. 3 shows the CO(1 – 0) LF at $z = 0$ for the hybrid GALFORM+UCL-PDR model, for the two parametrizations of G_{UV} : (i) $G_{\text{UV}}(\Sigma_{\text{SFR}})$ (Eq. 3) and (ii) $G_{\text{UV}}(\Sigma_{\text{SFR}}, Z_{\text{gas}}, \Sigma_{\text{gas}})$ (Eq. 4). We also show the latter model, (ii), without the inclusion of AGN as an ISM heating source. For reference, we also show the predictions of the GALFORM model without the processing of the PDR model, in the simplistic case where we assume two constant conversion factors, $X_{\text{CO}(1-0)} = 2 \times 10^{20} \text{ cm}^{-2} (\text{K km s}^{-1})^{-1}$ for quiescent galaxies and $X_{\text{CO}(1-0)} = 0.8 \times 10^{20} \text{ cm}^{-2} (\text{K km s}^{-1})^{-1}$ for starbursts. Observational estimates of the CO(1 – 0) LF made using both, *B*-band and 60 μm selected samples, are plotted as symbols (Keres et al. 2003).

Differences between the predictions of the model using different assumptions about G_{UV} become evident at CO luminosities brighter than the break in the CO LF (i.e. $\log(L_{\text{CO}}/\text{Jy km/s Mpc}^2) \approx 6.7$). The model assuming a dependence of G_{UV} solely on Σ_{SFR} predicts a larger number density of bright galaxies due to the higher G_{UV} values in galaxies with large molecular mass and high SFRs. We show later that the kinetic gas temperatures of the GALFORM+UCL-PDR model, when assuming a dependence of G_{UV} solely on Σ_{SFR} , are very high and also translate into unrealistic emission from higher order CO transitions. The values of G_{UV} are smaller when including the dependence on the optical depth, τ_{UV} , given that the increase in Σ_{SFR} is compensated by an increase in τ_{UV} , which brings G_{UV} down. This model predicts a LF which is closer to and in reasonable agreement

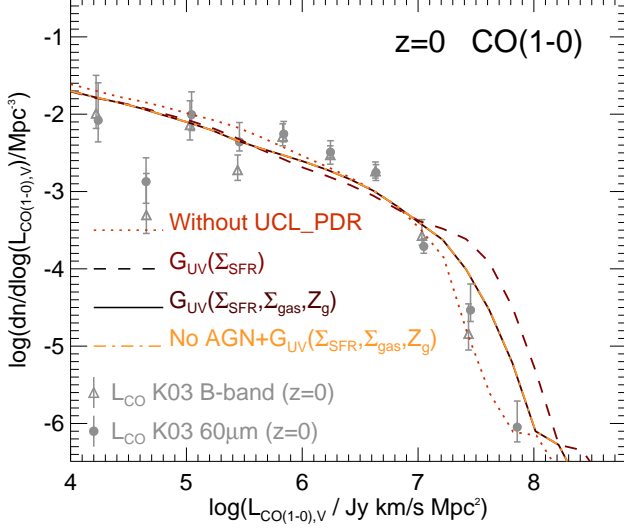


Figure 3. The $z = 0$ CO(1 – 0) luminosity function predicted by GALFORM+UCL_PDR model. Observational estimates of Keres et al. (2003) for samples of galaxies selected in the B -band (triangles) and at $60\,\mu\text{m}$ (filled circles), are also shown. The predictions of the models are shown for the GALFORM+UCL_PDR model when (i) $G_{\text{UV}} = G_{\text{UV}}(\Sigma_{\text{SFR}})$ (Eq. 3; dashed line), (ii) $G_{\text{UV}} = G_{\text{UV}}(\Sigma_{\text{SFR}}, Z_{\text{gas}}, \Sigma_{\text{gas}})$ (Eq. 4; solid line), and (iii) using G_{UV} as in (ii) but assuming AGN do not contribute to heat the ISM (dot-dashed line). For reference, we also show the predictions of the GALFORM model without the PDR coupling, assuming two constant X_{CO} factors, $X_{\text{CO}(1-0)} = (2, 0.8) \times 10^{20}\,\text{cm}^{-2}\,(\text{K km s}^{-1})^{-1}$ for quiescent and starburst galaxies, respectively (dotted line).

with the observations. When AGN are not included as a heating mechanism, the model predictions for the CO(1 – 0) LF are not affected, indicating that lower CO transitions are not sensitive to the presence of AGN. However, as we show later (Fig. 5), the emission in high CO transitions is very sensitive to the presence of an AGN. The GALFORM model without the PDR (i.e. using two ad hoc constant values of X_{CO} for starburst and quiescent galaxies) gives a LF closer to the observed number density of bright galaxies. This happens because galaxies in the bright-end of the CO LF mainly correspond to quiescent, gas-rich galaxies, whose $G_{\text{UV}} > G_0$, driving lower X_{CO} in the GALFORM+UCL_PDR model compared to the value typically assumed for quiescent galaxies ($X_{\text{CO}} = 2 \times 10^{20}\,\text{cm}^{-2}\,(\text{K km s}^{-1})^{-1}$).

The predictions of the GALFORM+UCL_PDR model using the form $G_{\text{UV}}(\Sigma_{\text{SFR}}, Z_{\text{gas}}, \Sigma_{\text{gas}})$ (Eq 4), give a reasonable match to the observational data from Keres et al. (2003). We remind the reader that the model has not been tuned to reproduce the CO LF. However, it is important to bear in mind that the CO LF from Keres et al. (2003) is not based on a blind CO survey, but instead on galaxy samples selected using $60\,\mu\text{m}$ or B -band fluxes. These criteria might bias the LF towards galaxies with large amounts of dust or large recent SF.

3.2 The CO-to-Infrared luminosity ratio

Fig. 4 shows the $L_{\text{CO}(1-0)}/L_{\text{IR}}$ ratio as a function of L_{IR} . Lines show the median of the GALFORM+UCL_PDR model predictions when using $G_{\text{UV}}(\Sigma_{\text{SFR}})$ (Eq. 3; dashed line) and $G_{\text{UV}}(\Sigma_{\text{SFR}}, Z_{\text{gas}}, \Sigma_{\text{gas}})$ (Eq. 4; solid line). Errorbars show the 10

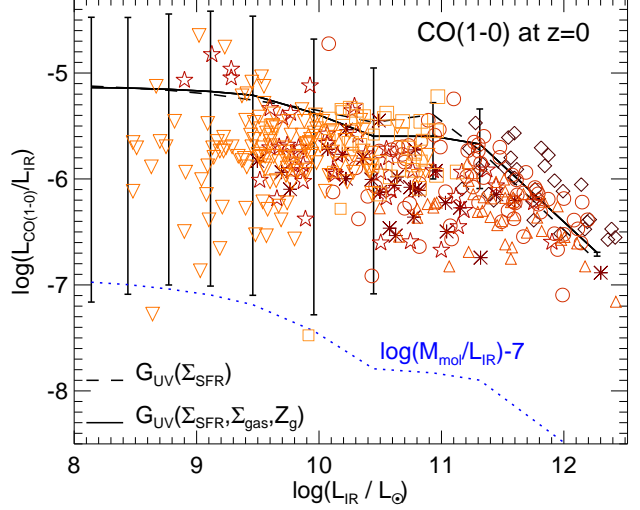


Figure 4. CO(1 – 0)-to-IR luminosity ratio as a function of IR luminosity. Lines show the median of the GALFORM+UCL_PDR model when G_{UV} is estimated from Eqs. 3 (dashed line) and 4 (solid line). Errorbars show the 10 and 90 percentiles of galaxies in the model, and for clarity, are only shown for the case of G_{UV} estimated from Eq. 4. For reference, we also show as dotted line the predictions of the L11 model for the molecular-to-IR luminosity ratio, $\log(M_{\text{mol}}/L_{\text{IR}} M_{\odot}/L_{\odot})$, shifted by an arbitrary factor of 7 dex. Observations from Young & Scoville (1991), Yao et al. (2003), Solomon et al. (1997), Bayet et al. (2009a), Papadopoulos et al. (2011), Rahman et al. (2012) and Lisenfeld et al. (2011) are shown as symbols.

and 90 percentiles of the distributions. We also show, for reference, the molecular mass-to-IR luminosity ratio, $M_{\text{mol}}/L_{\text{IR}}$, predicted by the L11 model and shifted by an arbitrary factor of 7 dex (dotted line). Symbols show an observational compilation of local LIRGs and ULIRGs.

The model predicts that the $L_{\text{CO}(1-0)}/L_{\text{IR}}$ ratio decreases as the IR luminosity increases. This trend is primarily driven by the dependence of the molecular mass-to-IR luminosity ratio on the IR luminosity which has the same form (dotted line). The trend of decreasing $M_{\text{mol}}/L_{\text{IR}}$ with increasing IR luminosity is driven by the gas metallicity-IR luminosity relation. Gas metallicity declines as the IR luminosity decreases (bottom panel of Fig. 1), which results in lower dust-to-total gas mass ratios and therefore lower IR luminosities for a given SFR. The molecular mass is not affected by gas metallicity directly since it depends on the hydrostatic pressure of the disk (see §2.1). Note that this effect affects galaxies with $L_{\text{IR}} < 5 \times 10^{10} L_{\odot}$, given that the gas metallicity-IR luminosity relation flattens above this IR luminosity (bottom panel of Fig. 1). The distributions of $L_{\text{CO}(1-0)}/L_{\text{IR}}$ predicted by the model extend to very low $L_{\text{CO}(1-0)}/L_{\text{IR}}$ ratios (as shown by the errorbars in Fig. 4). This is due to satellite galaxies in groups and clusters, which tend to have lower molecular mass-to-IR luminosity ratios, but that are relatively bright in IR due to their high gas metallicities (solar or supersolar), and therefore, large dust-to-gas mass ratios.

At $5 \times 10^{10} L_{\odot} < L_{\text{IR}} < 5 \times 10^{11} L_{\odot}$, the $L_{\text{CO}(1-0)}/L_{\text{IR}}$ - L_{IR} relation tends to flatten. This is due to a transition from galaxies dominated by quiescent SF to starburst galaxies, and the two different SF laws assumed in the model (see §2.1). The SF law determines how fast the cold gas is converted into stars, thus playing a key role in determining the molecular reservoir at a given time. In starburst galaxies, the SF timescale depends on the dy-

namical timescale of the bulge component with a floor (Eq. 2). Starburst galaxies, which largely contribute to the number density at $L_{\text{IR}} > 5 \times 10^{10} L_{\odot}$, have similar SF timescales given their similar properties in stellar mass and size, therefore resulting in, similar molecular-to-SFR ratios, except for the brightest ones with $L_{\text{IR}} > 5 \times 10^{11} L_{\odot}$. This effects dominates the behaviour of the $L_{\text{CO}(1-0)}/L_{\text{IR}}$ ratio, with a second order contribution from variations in X_{CO} , which tend to be small at these high gas surface densities (see Fig. 2). This prediction of the model explains what has been observed in local and a few high-redshift galaxies: variations in the CO-to-IR luminosity ratio are of the same order as the variations of molecular mass-to-IR luminosity ratios, as inferred from the dust emission (Leroy et al. 2011; Magdis et al. 2011). For the brightest galaxies, $L_{\text{IR}} > 5 \times 10^{11} L_{\odot}$, the SF timescale decreases rapidly with increasing IR luminosity and consequently, the molecular mass-to-IR luminosity ratio also decreases.

We conclude that the GALFORM+UCL-PDR model is able to explain the observed CO(1–0) emission of galaxies in the local Universe and its relation to the IR luminosity.

4 THE CO EMISSION OF GALAXIES IN MULTIPLE TRANSITIONS

We now focus on the predictions of the GALFORM+UCL-PDR model for the CO emission of galaxies in multiple CO lines in the local and high-redshift universe. We focus on the CO LF of galaxies, the relation between the CO and IR luminosity, and the CO SLED. In contrast to the case of the CO(1–0) transition, the available observational data for higher CO transitions are scarce and limited to individual objects, instead of homogeneous samples of galaxies. To carry out the fairest comparison possible at present, we select model galaxies in order to sample similar IR luminosity distributions to those in the observational catalogues.

4.1 The luminosity function of multiple CO lines

The top row of Fig. 5 shows the CO(1–0), CO(3–2) and CO(7–6) LFs at $z = 0$ for the GALFORM+UCL-PDR model using the scalings of $G_{\text{UV}}(\Sigma_{\text{SFR}})$ (Eq. 3) and $G_{\text{UV}}(\Sigma_{\text{SFR}}, Z_{\text{gas}}, \Sigma_{\text{gas}})$ (Eq. 4). The contributions from X-ray bright AGNs, with $L_{\text{X}} > 10^{44} \text{ s}^{-1} \text{ erg}$, and from quiescent and starburst galaxies with $L_{\text{X}} < 10^{44} \text{ s}^{-1} \text{ erg}$, are shown separately only for the model using $G_{\text{UV}}(\Sigma_{\text{SFR}}, Z_{\text{gas}}, \Sigma_{\text{gas}})$. Note that X-ray bright AGNs can correspond to both quiescent and starburst galaxies. The observational results for the CO(1–0) LF from Keres et al. (2003) at $z = 0$ and from Aravena et al. (2012) and Daddi et al. (2010) at $z = 2$ are also plotted in the top and bottom left-hand panels, respectively. The model using $G_{\text{UV}}(\Sigma_{\text{SFR}})$ predicts a higher number density of bright galaxies for the three CO transitions shown in Fig. 5 due to the fact that with this assumption, galaxies typically have a higher value of G_{UV} than in the parametrisation of Eq. 4, which leads to lower values of X_{CO} . The offset in the bright-end between the model predictions when using $G_{\text{UV}}(\Sigma_{\text{SFR}})$ and $G_{\text{UV}}(\Sigma_{\text{SFR}}, Z_{\text{gas}}, \Sigma_{\text{gas}})$ increases for higher CO transitions, since $J > 4$ CO transitions are more sensitive to changes in kinetic temperature, and therefore in G_{UV} . For $G_{\text{UV}}(\Sigma_{\text{SFR}})$, galaxies are on average predicted to be very bright in the CO(7–6) transition. As we show later, this model predicts an average CO(7–6) luminosity brighter than observed for local LIRGs (see Fig. 6 in §4.2.1), but still consistent with the observations within the errorbars. Quiescent galaxies in the model are responsible for shaping the faint end

of the CO LF, regardless of the CO transition. Starburst galaxies make a very small contribution to the CO LFs at $z = 0$, given their low number density.

Galaxies which host a X-ray bright AGN are an important contributor to the bright-end of the CO LF, along with normal star-forming galaxies, regardless of the transition. In the case of the CO(1–0) and CO(3–2) transitions, this is not due to the presence of the AGN in these galaxies, but instead to the large molecular gas reservoir, the typically high gas metallicities, and the high SFRs, which on average produce higher G_{UV} , and therefore more CO luminosity per molecular mass. The powerful AGN is therefore a consequence of the large gas reservoirs, which fuel large accretion rates, along with a massive central black hole, and has only a secondary effect through increasing the kinetic temperature, that is not enough to produce a visible effect on the low CO transitions. However, the CO(7–6) transition is slightly more sensitive to variations in the kinetic temperature of the gas, as we show in §4.2. The contribution from bright AGN and quiescent galaxies to the bright-end of the CO LF at $z = 0$ is very similar, regardless of the CO transition. This is due to the X-ray luminosity threshold chosen to select AGN bright galaxies, $L_{\text{XR}} > 10^{44} \text{ erg s}^{-1}$, which takes out most of quiescent galaxies in the bright-end of the CO LF, which have hard X-ray luminosities in the range $10^{43} < L_{\text{XR}}/\text{erg s}^{-1} < 10^{44}$.

The bottom row of Fig. 5 is the same as the top row but shows the LFs at $z = 2$. In this case we only show the predictions of the GALFORM+UCL-PDR model in the G_{UV} approximation of Eq. 4. To illustrate evolution between $z = 0$ and $z = 2$, the dotted straight lines show the number density of galaxies at $z = 0$ with a luminosity of $10^7 \text{ Jy km/s Mpc}^2$ in the different CO transitions. Bright CO galaxies are more common at $z = 2$, which is reflected in the higher number density of galaxies with $L_{\text{CO,V}} > 10^7 \text{ Jy km/s Mpc}^2$ compared to $z = 0$. Bright AGNs, which are more common and brighter at $z = 2$ than at $z = 0$, are responsible for most of the evolution in the bright-end of the CO LF with redshift, with a less important contribution from quiescent and starburst galaxies that host fainter AGN. In the faint-end, there is an significant increase in the number density of galaxies, driven by the evolution of quiescent galaxies. In general, the LF for higher CO transitions shows stronger evolution with redshift than it does for lower CO transitions, again indicating that the higher CO transitions are more sensitive to variations in G_{UV} and F_{X} . From an observational point of view, measuring CO luminosity ratios, such as the CO(7–6)-to-CO(1–0) ratio, is promising for constraining the average physical state of the molecular gas. However, in terms of estimating the total molecular mass in galaxies, lower CO transitions are more useful, given their lower sensitivity to changes in the conditions in the ISM in galaxies. Our predictions for the CO(1–0) at $z = 2$ agree very well with the observed number density of bright CO(1–0) galaxies reported by Daddi et al. (2010) and Aravena et al. (2012). However, the uncertainty in the inferred space density displayed by the observations at $z = 2$ is large, suggesting that further observations, desirably from CO blind surveys, are necessary to put better constraints in the CO LF.

Our predictions for the LF show that intermediate CO transitions are brighter in units of the velocity-integrated CO luminosity than lower and higher order CO transitions. This trend is similar to the predictions of Obreschkow et al. (2009), who used a completely different approach, which relied on estimating a gas temperature based on the SFR surface density or AGN bolometric luminosity under local thermodynamic equilibrium (i.e. a single gas phase). However, Obreschkow et al. predict a significant decrease in the

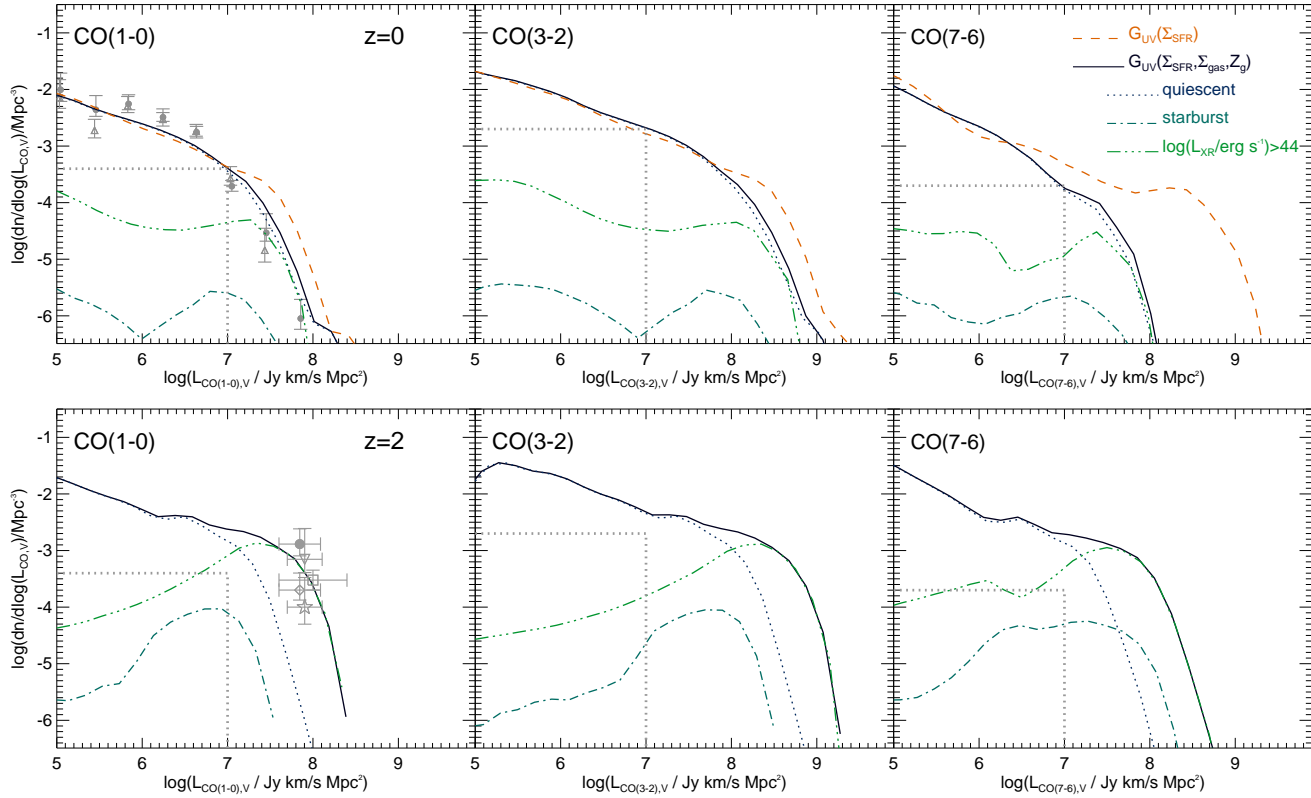


Figure 5. *Top Row:* The CO(1 – 0) (left-hand panel), CO(3 – 2) (middle panel) and CO(7 – 6) (right-hand panel) luminosity functions at $z = 0$ predicted by the GALFORM+UCL_PDR model. In the left-hand panel, the observational estimates of Keres et al. (2003) are shown as in Fig. 3. The solid and dashed lines show the predictions for the two different assumptions used to estimate G_{UV} , Eqs. 3 and 4, respectively. We use the predictions of the model using the G_{UV} parametrisation of Eq. 4 to show the contributions to the LF from starburst galaxies (dot-dashed lines) and normal star-forming galaxies (dotted) without a bright AGN, and galaxies which host a bright AGN (X-ray luminosities $L_X > 10^{44} \text{ erg s}^{-1}$; triple-dot-dashed line). *Bottom Row:* The same as the top row but at $z = 2$. In this set of plots we only show the predictions of the model using the G_{UV} of Eq. 4. In the left-hand panel, the observational estimates of Aravena et al. (2012) and Daddi et al. (2010) are shown in symbols. The solid circle and empty diamond correspond to the observational data of Aravena et al. without and with correction for the overdensity of the field, respectively, while the empty triangle and square show the estimates of the number density when only galaxies with spectroscopically confirmed redshifts are considered, without and with correction for the overdensity of the field, respectively. The empty star corresponds to the estimate of Daddi et al. (2010). To show the evolution in the LF, the dotted straight lines show the number density of galaxies at a CO luminosity of $10^7 \text{ Jy km/s Mpc}^2$ at $z = 0$ in both sets of rows.

number density of faint CO galaxies as the upper level J increases, behaviour that is not seen in our model. A possible explanation for this is that their model assumes local thermodynamic equilibrium, for which high order CO transitions would be thermalised. This, in addition to the parameters Obreschkow et al. use to estimate L_{CO} , can lead to much lower CO emission in high- J transitions compared to that in our model. For example at $T_K = 10 \text{ K}$, and using the equations and parameters given in Obreschkow et al., a ratio of $L_{CO(7-6),V}/L_{CO(1-0),V} \approx 10^{-3}$ is obtained, while our model predicts $L_{CO(7-6),V}/L_{CO(1-0),V} \approx 0.1$ for the same temperature. Our approach does not require any of these assumptions given that the PDR model is designed to represent much more accurately the excitation state of GMCs.

In general, the GALFORM+UCL_PDR model predicts a higher number density of bright galaxies at high-redshifts, a trend which is slightly more pronounced for the higher CO transitions. For low CO transitions, the main driver of this effect is the higher number density of galaxies with large molecular gas reservoirs at high redshift (see Lagos et al. 2011a). For high CO transitions what makes the effect stronger is the higher average kinetic temperatures of the gas in molecular clouds at high redshifts (see Fig. 10).

4.2 The CO-to-IR luminosity ratio and the CO SLED

In this section we study the CO-to-IR luminosity ratio for multiple CO lines and compare to observational data in the local and high redshift Universe.

4.2.1 The CO-to-IR luminosity ratio and CO SLED in the local universe

Observations have shown that emission from multiple CO transitions can help to constrain the state of the ISM in galaxies through the comparison with the predictions of PDR and LVG models. In the local Universe, around 100 galaxies have been observed in more than one CO transition. However, the one caveat to bear in mind is the selection of these samples, as they are built from studies of individual galaxies and are, therefore, inevitably biased towards bright galaxies. To try to match the composition of the observational sample, we select galaxies from the model with the same distribution of IR luminosities as in the observed samples. In this section we present this comparison, which allows us to study whether or not the model predicts galaxies that reproduce the observed CO ladder.

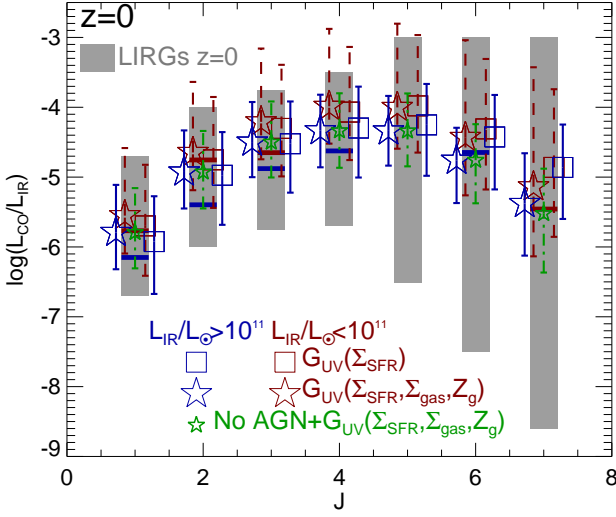


Figure 6. CO($J \rightarrow J - 1$) to IR luminosity ratio as a function of upper level J at $z = 0$. Grey solid bars show the range of observed ratios reported by Papadopoulos et al. (2011) for 70 LIRGs at $z \leq 0.1$. Horizontal segments show the median in the observed data for two IR luminosity bins, $L_{\text{IR}}/L_{\odot} < 10^{11}$ (dark red with errorbars as dashed lines) and $L_{\text{IR}}/L_{\odot} > 10^{11}$ (blue with errorbars as solid lines). We show as symbols the predictions of a sample of model galaxies randomly chosen to have the same IR luminosity distribution as the Papadopoulos et al. sample. Symbols and errorbars correspond to the median and 10 and 90 percentiles of the predictions for the GALFORM+UCL-PDR model using the G_{UV} parametrisations of Eqs. 3 (squares) and 4 (large stars). For reference we also show for the bright IR luminosity bin the predictions of the model using G_{UV} from Eq. 4 when AGN are not considered as an ISM heating mechanism (small stars).

We compare the model predictions with the observational catalogue presented in Papadopoulos et al. (2011). This sample comprises 70 LIRGs and ULIRGs at $z \leq 0.1$ which have the emission of several CO transitions measured, as well as other molecular species. The IR luminosities of these galaxies cover the range $10^{10} - 5 \times 10^{12} L_{\odot}$. We randomly select galaxies in the model at $z = 0$ to have the same distribution of IR luminosities as the sample of Papadopoulos et al. (2011).

Fig. 6 shows the predicted CO-to-IR luminosity ratio for different transitions compared to the observational data, in two bins of IR luminosity, $10^{10} < L_{\text{IR}}/L_{\odot} < 10^{11}$ and $10^{11} < L_{\text{IR}}/L_{\odot} < 5 \times 10^{12}$. In the case of the observations, gray bands show the whole range of observed CO-to-IR luminosity ratios, while the horizontal segments show the medians of the bright (blue) and faint (dark red) IR luminosity bins. In the case of the model, we show the medians and 10 and 90 percentiles of the distributions as symbols and errorbars, respectively, where dark red and blue symbols corresponds to the low and high luminosity bins, respectively. Model predictions are presented for the two parametrisations of G_{UV} discussed in §3.1.1 (see Eqs. 3-4). We also show for the bright IR luminosity bin, the CO-to-IR luminosity ratios for the model using $G_{\text{UV}}(\Sigma_{\text{SFR}}, Z_{\text{gas}}, \Sigma_{\text{gas}})$ (Eq. 4) and assuming no heating of the ISM by AGN (small stars). The model predicts $L_{\text{CO}}/L_{\text{IR}}$ ratios which are well within the observed ranges. For higher CO transitions, the model predicts broader distributions of the $L_{\text{CO}}/L_{\text{IR}}$ ratio than at low CO transitions, independent of the G_{UV} parametrisation. The model also predicts that galaxies in the bright IR lumi-

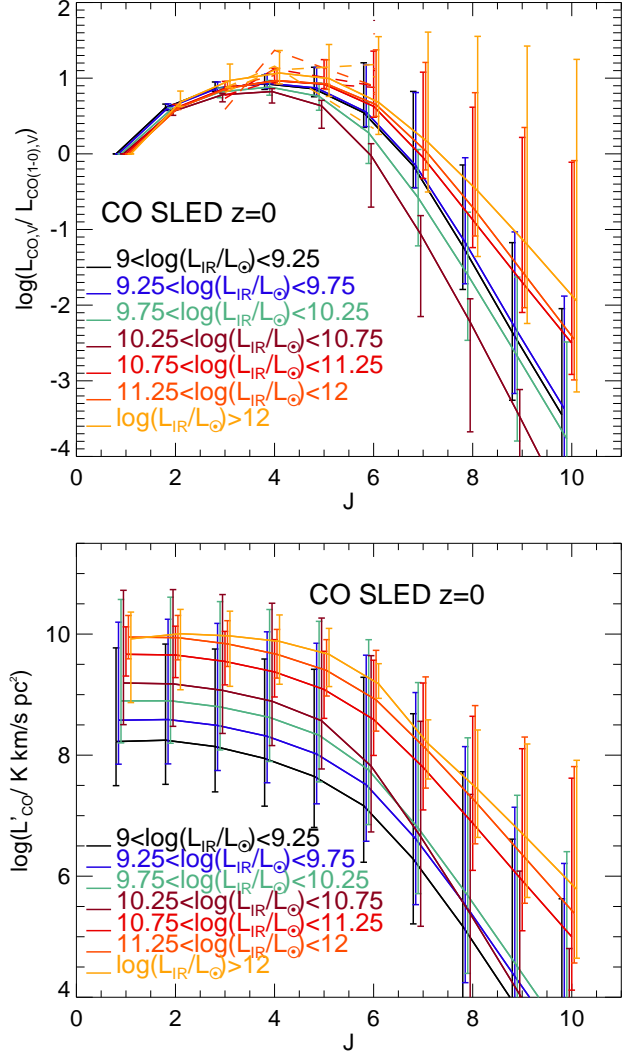


Figure 7. *Top panel:* The velocity-integrated luminosity normalized to the CO(1 – 0) luminosity as a function of the upper quantum level of the CO rotational transition, J , predicted by the GALFORM+UCL-PDR model at $z = 0$ for galaxies with IR luminosities in different ranges, as labelled, and using the G_{UV} parametrisation of Eqs. 4. Solid lines and errorbars show the medians and 10 and 90 percentile ranges of the distributions. Dashed lines show individual galaxies from the Papadopoulos et al. (2011) observational sample, following the same colour code as the model galaxies. *Bottom panel:* Brightness temperature luminosity, L'_{CO} , as a function of J for galaxies with IR luminosities in different ranges, as labelled. Note that $L'_{\text{CO}(1-0)}$ monotonically increases with IR luminosity.

nosity bin have slightly lower $L_{\text{CO}}/L_{\text{IR}}$ ratios compared to galaxies in the faint IR luminosity bin.

The two parametrisations of G_{UV} predict $L_{\text{CO}}/L_{\text{IR}}$ ratios that are only slightly offset, except for the highest CO transitions, $J > 5$, where the predictions differ by up to ≈ 0.5 dex. At $J > 5$, the model in which G_{UV} depends on the average UV optical depth, $G_{\text{UV}}(\Sigma_{\text{SFR}}, Z_{\text{gas}}, \Sigma_{\text{gas}})$, predicts on average $L_{\text{CO}}/L_{\text{IR}}$ ratios in better agreement with the observations than those predicted by the G_{UV} depending solely on Σ_{SFR} . This is due to the fact that galaxies with very high Σ_{SFR} , which drives high UV production, also tend to have high $Z_{\text{gas}} \Sigma_{\text{gas}}$, decreasing the UV ionizing background if the average UV optical depth is considered. For lower

CO transitions, the difference between the predictions of the model when G_{UV} is estimated as in Eqs. 3 and 4, becomes more evident for galaxies that are bright in CO, which affects the bright end of the CO luminosity function, as discussed in §3.1. Galaxies in the fainter IR luminosity bin correspond primarily to normal star-forming galaxies with $G_{UV}/G_0 \approx 1 - 10$, while galaxies in the brighter IR luminosity bin are a mixture of normal star-forming and starburst galaxies. The range of G_{UV} in these galaxies varies significantly. Starburst galaxies usually have larger G_{UV} in the range $G_{UV}/G_0 \approx 10 - 10^3$. Faint IR galaxies in the model, with $L_{IR} < 10^9 L_\odot$, can also correspond to passive galaxies, whose UV ionizing background is very small, $G_{UV}/G_0 \approx 0.01 - 1$.

The variation in G_{UV} within the faint and bright IR luminosity bins has a direct consequence on the range of gas kinetic temperatures displayed by galaxies in each bin. Galaxies in the faint IR bin have $T_K \approx 10 - 20$ K, while galaxies in the bright IR bin have $T_K \approx 10 - 60$ K. The presence of an AGN also has an effect on the kinetic temperature of the gas, and therefore on the CO emission of galaxies, as seen from the small stars in Fig. 6. When assuming that the AGN does not heat the ISM of galaxies, galaxies appear to have lower CO-to-IR ratios for $J > 6$ transitions by a factor ≈ 1.7 , while lower transitions are largely unaffected. This indicates again that high CO transitions are useful to constrain the effect of AGN in heating the ISM.

Fig. 7 shows the CO SLED in units of velocity-integrated CO luminosity, $L_{CO,V}$ (top panel), and brightness temperature luminosity, L'_{CO} (bottom panel), for $z = 0$ galaxies with IR luminosities in different luminosity bins, as labelled. Individual galaxies from the Papadopoulos et al. (2011) observational sample of LIRGs are shown as dashed lines in the top panel of Fig. 7. A typical way to show the CO SLED is velocity-integrated luminosity normalised by $L_{CO(1-0),V}$, given that this way the SLED shows a peak, which indicates the degree of excitation: the higher the J of the peak, the higher the gas kinetic temperature of molecular clouds, which typically indicates more SF and/or AGN activity (e.g. Weiß et al. 2007). When the CO SLED is shown in brightness temperature luminosity there is no clear peak (bottom panel of Fig. 7). This happens because $L_{CO,V}$ and L'_{CO} have different dependencies on J (see Appendix A). The GALFORM+UCL-PDR model predicts a peak in the CO SLED at $J = 4$ for galaxies with $L_{IR} \lesssim 10^{11} L_\odot$ and at $J = 5$ for galaxies with $L_{IR} \gtrsim 10^{11} L_\odot$, due to the starburst nature of the latter. We find that the lowest IR luminosity bin, $10^9 < L_{IR}/L_\odot < 1.7 \times 10^9$, shows a peak at higher J values, closer to starburst galaxies. This is due to the lower gas metallicities of these galaxies which increases G_{UV} and T_K . Our predictions agree with the observed peaks of LIRGs (dashed lines). However, we remind the reader that the LIRG catalogue of Papadopoulos et al. (2011) is not a statistically complete sample. Further observations are needed to construct volume-limited samples of galaxies with CO measurements in order to better constrain the physics of the ISM.

4.2.2 Redshift evolution of the CO-to-IR luminosity ratio and the CO SLED at high redshift

At high redshifts, observational data on the CO emission from galaxies is based on studies of individual galaxies, typically LIRGs, ULIRGs, QSOs and SMGs. This has allowed the characterisation of the CO-to-IR luminosity ratio for bright normal star-forming and starburst galaxies. In this section we compare these observations with the predictions of the GALFORM+UCL-PDR model.

Fig. 8 shows the redshift evolution of the L_{CO}/L_{IR} luminos-

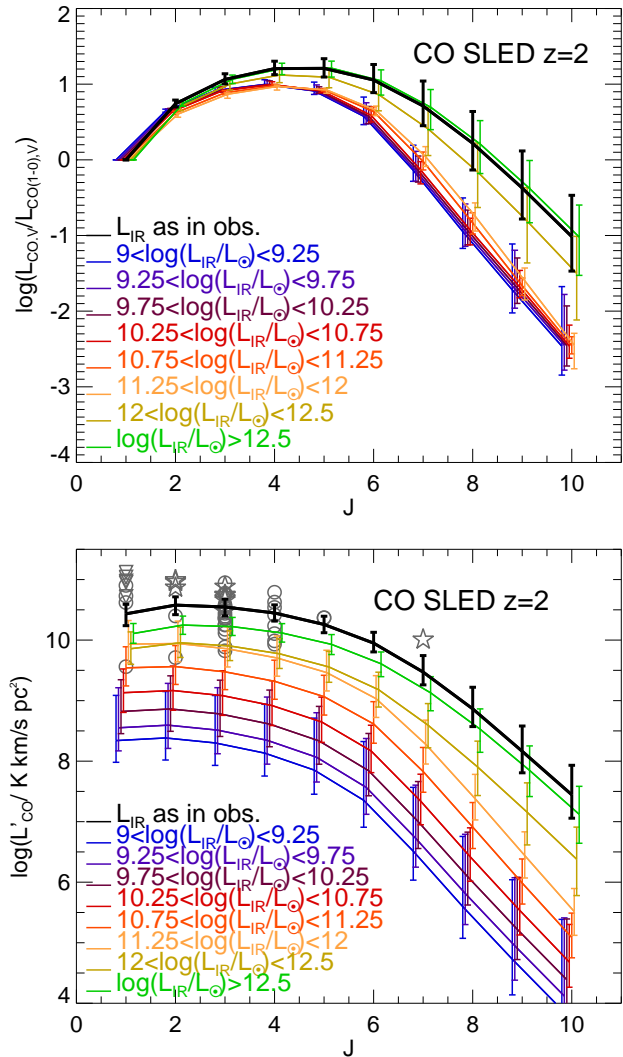


Figure 9. As in Fig. 7, but at $z = 2$. In the bottom panel we also show individual observations of SMGs from Frayer et al. (1998,1999), Neri et al. (2003), Sheth et al. (2004), Greve et al. (2005), Tacconi et al. (2006), Casey et al. (2009), Bothwell et al. (2010), Engel et al. (2010) and Ivison et al. (2011), which have a median redshift of $z \approx 2$. Symbols for these different sets of data are as in the bottom row of Fig. 8. In order to infer a typical CO SLED of SMGs, we have scaled their CO luminosities to a common IR luminosity, assuming that the observed L'_{CO}/L_{IR} is conserved (see text for details). We choose to scale the CO luminosities to the median IR luminosity of the sample, $\langle L_{IR} \rangle \approx 8 \times 10^{12} L_\odot$. We also show as a black solid line the predictions of the GALFORM+UCL-PDR model for a sample of model galaxies selected to have the same IR luminosity distribution as the compilation of observed SMGs, whose CO luminosities have been scaled in the same way as was done in the observational sample. Note that $L'_{CO(1-0)}$ monotonically increases with IR luminosity

ity ratio for model galaxies for four different CO transitions, in different bins of IR luminosity. Quiescent and starburst galaxies are shown separately in the top and bottom rows, respectively. We also show a large compilation of observational results of local and high redshift normal star-forming galaxies, local LIRGs, local ULIRGs, high redshift colour selected galaxies, SMGs, and local and high redshift QSOs, and plot them in the panel corresponding to the CO transition that was studied in each case. We plot observed CO-to-

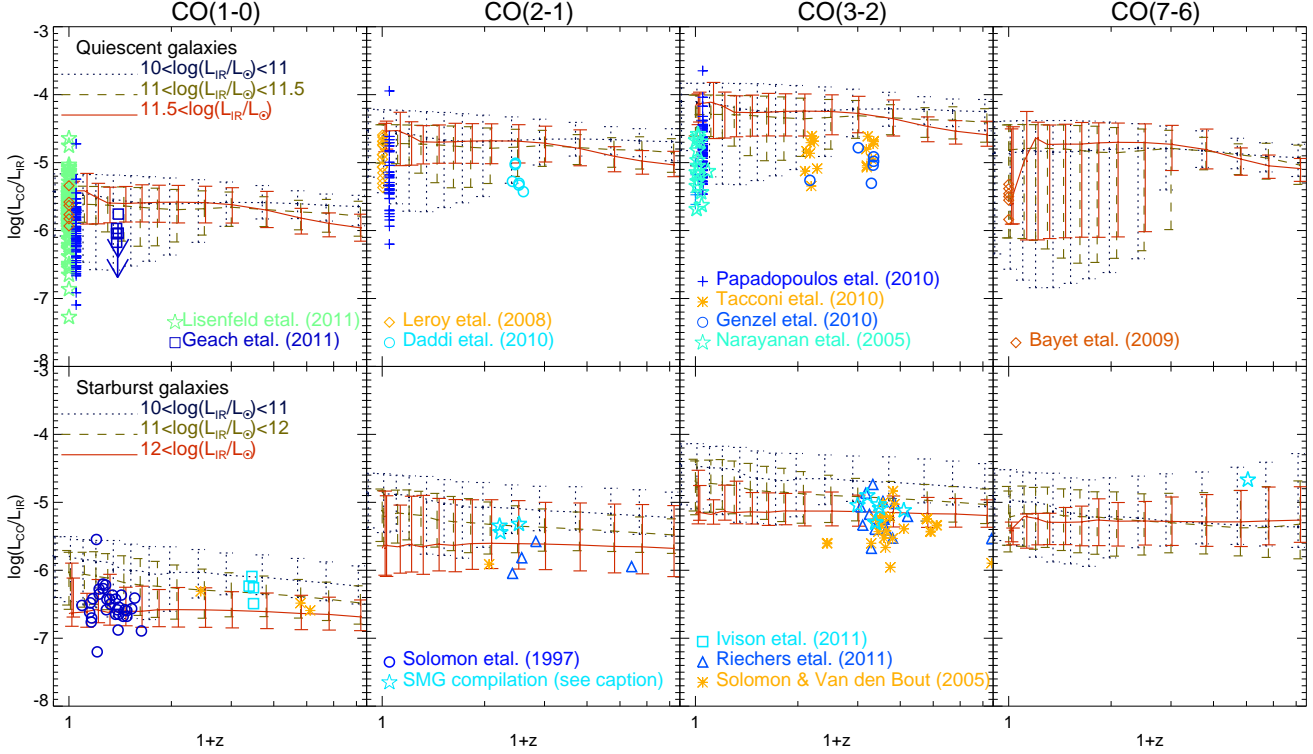


Figure 8. *Top Row:* CO-to-IR luminosity ratio as a function of redshift for quiescent galaxies in the GALFORM+UCL_PDR model and for four CO transitions, CO(1 – 0) (left-hand panel), CO(2 – 1) (middle-left panel), CO(3 – 2) (middle-right panel) and CO(7 – 6) (right-hand panel), for IR luminosities in different ranges, as shown in the label. Lines and errorbars represent the predicted median $L_{\text{CO}}/L_{\text{IR}}$ and the 10 and 90 percentiles of the distributions. Also shown are the following observational data: local normal spiral galaxies from Leroy et al. (2008) (diamonds), Lisenfeld et al. (2011) (stars), Bayet et al. (2009a) (diamonds); LIRGs from Narayanan et al. (2005) (stars) and Papadopoulos et al. (2011) (crosses); star-forming galaxies at $z \approx 1.2$ and $z \approx 2.3$ from Tacconi et al. (2010) (asterisks) and Genzel et al. (2010) (circles); normal star-forming galaxies, BzK selected, from Daddi et al. (2010) (circles); normal star-forming galaxies at intermediate redshifts from Geach et al. (2011) (squares). Arrows indicate upper limits of IR sources with no detections of CO. *Bottom Row:* the same as the top row, but for starburst galaxies. Also shown are the observational results for ULIRGs from Solomon et al. (1997) (circles), SMG from Solomon & Vanden Bout (2005) (asterisks; which compiled the SMG data from Frayer et al. 1998, 1999, Neri et al. 2003, Sheth et al. 2004, Greve et al. 2005), Ivison et al. (2011) (squares) and a compilation including Tacconi et al. (2006), Casey et al. (2009), Bothwell et al. (2010) and Engel et al. (2010) (stars), and QSOs from Riechers (2011) (triangles). We remind the reader that most of the observational data plotted here do not directly measure total IR luminosity, but infer it from an estimated SFR or from mid-IR or the submillimeter emission (see text for details).

IR luminosity ratios in the top rows of Fig. 8 if observed galaxies correspond to normal star-forming galaxies or LIRGs, or in the bottom row if they are classified as starburst galaxies (ULIRGs, SMGs or QSOs). We warn the reader that most of the observational data do not directly measure total IR luminosity, but infer it from either the emission in mid-IR or sub-millimeter bands, such as $24\mu\text{m}$ or $850\mu\text{m}$, or an observationally inferred SFR. Thus, the comparison between the model predictions and the observations in Fig. 8 has to be done with care.

There is a weak trend of lower $L_{\text{CO}}/L_{\text{IR}}$ ratios as L_{IR} increases in both galaxy types as was shown at $z = 0$ in Fig. 4. In the case of quiescent galaxies, this trend is driven by the gas metallicity: IR faint galaxies have lower metallicities, which, on average, decrease the dust opacity and the corresponding IR luminosity, producing higher $L_{\text{CO}}/L_{\text{IR}}$ ratios. In the case of starburst galaxies, the main driver of the decreasing $L_{\text{CO}}/L_{\text{IR}}$ ratio with increasing L_{IR} is the accompanying decrease in molecular mass for a given SFR due to the dependence of the SF law on the dynamical timescale of the bulge in starbursts. This reduces the SF timescale in the most massive and brightest galaxies.

Observations shown in the panels corresponding to quiescent galaxies at intermediate and high redshifts show galaxies se-

lected through different methods: Geach et al. (2011) measured the CO(1 – 0) emission in a $24\mu\text{m}$ -selected sample at $z \approx 0.4$ of galaxies infalling into a rich galaxy cluster, Daddi et al. (2010) measured the CO(2 – 1) emission in a colour-selected sample of galaxies (BzK; see §6.1), and Tacconi et al. (2010) and Genzel et al. (2010) measured CO(3 – 2) in a sample of normal star-forming galaxies located on the star forming sequence of the SFR – M_{stellar} plane. In the case of Daddi et al. (2010), Tacconi et al. (2010) and Genzel et al. (2010), IR luminosities are inferred from the SFR, which in turn is estimated from the rest-frame UV and mid-IR emission with an uncertainty of a factor ≈ 2 . The conversion between SFR and IR luminosity used in these works corresponds to the local Universe relation calibrated for solar metallicity. High-redshift galaxies tend to have lower metallicities (e.g. Mannucci et al. 2010; Lara-López et al. 2010), for which the use of the local Universe relation could possibly lead to an overestimate of the IR luminosity, and therefore, an underestimate of the $L_{\text{CO}}/L_{\text{IR}}$ ratio. Given this caveat, the apparent discrepancy of ≈ 0.3 dex between the model predictions and the high redshift observations does not seem to be critical. Accurate IR luminosity measurements for high redshift galaxies are needed to better assess how the model predictions compare with the observations.

In the case of starbursts, observations correspond to the brightest galaxies observed in the local and high redshift Universe. IR luminosities for these galaxies are usually inferred from far-IR or sub-mm bands, e.g. $850\ \mu\text{m}$, and they are predicted to have gas metallicities close to solar, for which uncertainties in the IR luminosity are expected to be less important than in normal star-forming galaxies. These bright galaxies should be compared to the model predictions for the brightest IR galaxies. The model predicts a mean $L_{\text{CO}}/L_{\text{IR}}$ ratio and its evolution in good agreement with observations. These galaxies in the model are predicted to have gas kinetic temperatures of $\approx 50\ \text{K}$ (see red lines in Fig. 10).

Fig. 9 is similar to Fig. 7, but shows the CO SLED at $z = 2$. The redshift is chosen to match the median of the SMG observational compilation also shown in Fig. 9. This catalogue comprises 50 SMGs observed in various CO transitions with IR luminosities in the range $L_{\text{IR}} \approx 10^{12} - 4 \times 10^{13}\ L_{\odot}$. In order to infer a typical CO SLED of SMGs, we scale the CO luminosities in the SMG observational catalogue to the median IR luminosity of the sample, $\langle L_{\text{IR}} \rangle \approx 8 \times 10^{12}\ L_{\odot}$. We do this by assuming that the $L'_{\text{CO}}/L_{\text{IR}}$ ratio for a given source is conserved. Thus, the L'_{CO} plotted in Fig. 9 corresponds to the observed CO luminosity scaled by a factor $L_{\text{IR}}/\langle L_{\text{IR}} \rangle$. These scaled observations are shown as symbols in the bottom panel of Fig. 9. With the aims of performing a fair comparison to the model predictions, we select galaxies in the model to have the same IR luminosity distribution as the observational sample and then scale their CO luminosities following the same procedure as with the observations. This is shown as the black solid line in Fig. 9. The CO lines with the best statistics in the observational sample are the CO(1–0), CO(2–1), CO(3–2) and CO(4–3). The latter three correspond to the ones the model matches the best. In the case of the CO(1–0), there is a slight discrepancy between the model and the observations, but still consistent with the dispersion predicted by the model. At higher-J values, there are only two observations, one in agreement and the other one slightly above the model predictions. However, the low number statistics prevents us from determining how representative these points are of the general SMG population. The model predicts the peak of the CO SLED occurs, on average, at $J = 5$ for these very luminous IR galaxies.

For the general galaxy population, the model predicts that the brightest IR galaxies have slightly flatter CO SLEDs than fainter IR counterparts. Differences in the CO SLEDs of faint- and bright-IR galaxies at $z = 2$ are predicted to be smaller than for $z = 0$ galaxies. In other words, at a fixed IR luminosity, high redshift galaxies tend to have shallower CO SLEDs compared to their $z = 0$ counterparts. This is due to a tendency of increasing average gas kinetic temperature in molecular clouds with increasing redshift (see Fig. 10), driven by the systematically lower metallicities and higher SFR surface densities of high redshift galaxies.

4.2.3 Kinetic temperature evolution

The variation of the $L_{\text{CO}}/L_{\text{IR}}$ luminosity ratio with IR luminosity differs between quiescent and starburst galaxies, and is related to variations in the gas kinetic temperature, which depend on IR luminosity and redshift. Fig. 10 shows the gas kinetic temperature of molecular clouds for quiescent (blue lines) and starburst (red lines) gas phases for different IR luminosity bins, as a function of redshift. For reference, we also show the evolution of the temperature of the Cosmic Microwave Background (CMB) with redshift. Note that some galaxies undergoing quiescent SF appear to have kinetic temperatures below the CMB temperature at $z \gtrsim 4.5$. For these galaxies, extra heating from the CMB needs to be in-

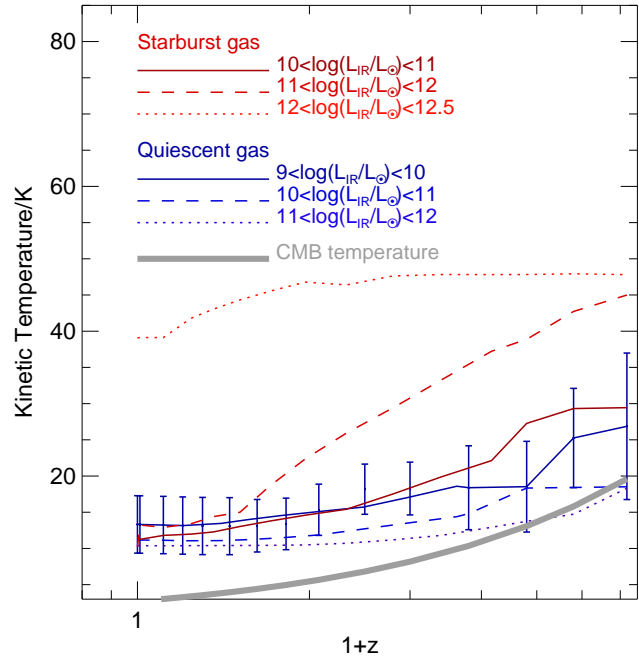


Figure 10. Kinetic temperature of the gas in molecular clouds for quiescent (blue curves) and starburst (red curves) gas phases in the ISM of galaxies as a function of redshift and for various bins of IR luminosity, as labelled. Lines show the median of the predicted T_K , while errorbars correspond to the 10 and 90 percentile range. For clarity errorbars are only shown in one IR luminosity bin for the quiescent gas phase. For reference, the Cosmic Microwave Background temperature is shown as a thick grey solid line. Note that galaxies can have SF taking place simultaneously in the galactic disk and the bulge, for which they would have two gas phases, a quiescent and a starburst gas phase, respectively. For the same line style, starbursts have higher T_K than quiescent gas in galaxies.

cluded in the UCL-PDR model to describe the thermal and chemical state of these galaxies. This represents a limitation of the current GALFORM+UCL-PDR model. However, this only becomes relevant at very high redshift and for quiescent galaxies.

The relation between the kinetic temperature of the gas and IR luminosity is primarily dominated by gas metallicity in quiescent galaxies and by the UV radiation field in starburst galaxies. In the case of quiescent galaxies, the gas metallicity increases as the IR luminosity increases, and therefore the gas cools more efficiently, decreasing T_K as L_{IR} increases. This is true only in this quiescent regime given that G_{UV} only varies around $1 - 10 \times G_0$. In the case of starburst galaxies, as the IR luminosity increases so does the UV radiation field, G_{UV} , which boosts the kinetic temperature of the gas, driving a positive relation between T_K and L_{IR} .

In general, starburst galaxies tend to have higher T_K than quiescent galaxies. The GALFORM+UCL-PDR model predicts that both cool and a warm ISM phases should be present in the high redshift universe, particularly in relatively bright galaxies (but not exclusively in the brightest ones), given that a large fraction of galaxies in the model at high redshift have SF taking place simultaneously in both the disk and bulge components.

5 ASSESSING THE ROBUSTNESS OF THE MODEL PREDICTIONS

We analyse in this section how the predictions of the coupled model presented in §3 and §4 depend on the assumptions made in the PDR model. We focus on (i) the effect of metallicity, and (ii) the effect of a varying hydrogen number density (as opposed to the fixed density adopted previously). For a detailed analysis on how other assumptions in the PDR modelling affect the results, e.g. the assumed geometry, see Röllig et al. (2007).

We have shown that gas metallicity has an important effect on the predicted CO luminosity and SLED, particularly for relatively IR-faint galaxies. These variations with metallicities have been extensively analysed in PDR and LVG models, such as in Wolfire et al. (2003), Bell et al. (2006) and Weiß et al. (2007). However, comparisons between observations and PDR or LVG models with the aim of inferring average GMC properties tend to ignore the metallicity effect by assuming that the metallicity is fixed at solar or super-solar (e.g. Hirschfeld et al. 2008; Danielson et al. 2010; Nagy et al. 2012). In order to assess how much our predictions change if we ignore changes in metallicity we perform the same calculations as in §4 but ignore the metallicity information in GALFORM. We therefore select the subset of the PDR models shown in Table 1 that have $Z_g = 1 Z_\odot$ and calculate the X_{CO} for each galaxy from that subset, regardless of its actual metallicity.

Fig. 11 shows the ratio between the predicted CO luminosity in the standard GALFORM+UCL_PDR model and the variant with a fixed gas metallicity, for 4 CO transitions and two IR luminosity ranges. Low CO transitions ($J \leq 4$) are only slightly affected by this change in the PDR models, with differences of less than a factor 3. IR bright galaxies show the least variation in CO luminosity with respect to the standard model due to their already high gas metallicities, which tend to be close to solar or super-solar. The CO luminosities of fainter galaxies in the IR are more affected given that they show larger gas metallicity differences, as Fig. 1 shows. As we move to higher CO transitions, differences with respect to the standard model increase to up to a factor ≈ 10 . This is driven by the generally larger variation of the population level of high CO transitions with cloud properties, as we described in §4. These results indicate that to assume a gas metallicity for observed galaxies might lead to a misinterpretation of the data, particularly when analysing high CO transitions. This effect has also been previously seen in detailed ISM hydro-dynamical simulations, such as in Feldmann et al. (2012).

Throughout the paper we have so far assumed that GMCs are characterised by a constant hydrogen density of $n_H = 10^4 \text{ cm}^{-3}$, which, we have shown, allows us to explain the observed CO luminosities of local and high-redshift galaxies. However, it is interesting to study the impact of allowing the hydrogen number density, n_H , to vary. This is because simulations and theoretical models suggest that a minimum density of hydrogen in GMCs is required to assure pressure equilibrium between a thermally supported warm medium and a turbulence supported cold neutral medium (Wolfire et al. 2003; Krumholz et al. 2009a). This minimum density depends on the UV flux, hard X-ray flux and metallicity as described by Wolfire et al. (2003),

$$n_{H,\min} \propto \frac{G_{\text{UV}}}{1 + 3.1(G_{\text{UV}} Z_g F_X)^{0.37}}, \quad (7)$$

where $n_{H,\min}$, G_{UV} , Z_g and F_X are in units of cm^{-3} , G_0 , Z_\odot and $10 \text{ erg s}^{-1} \text{ cm}^{-2}$ (following our conversion between F_X and ζ_0 described in §2.2). We explore the effect of assuming that

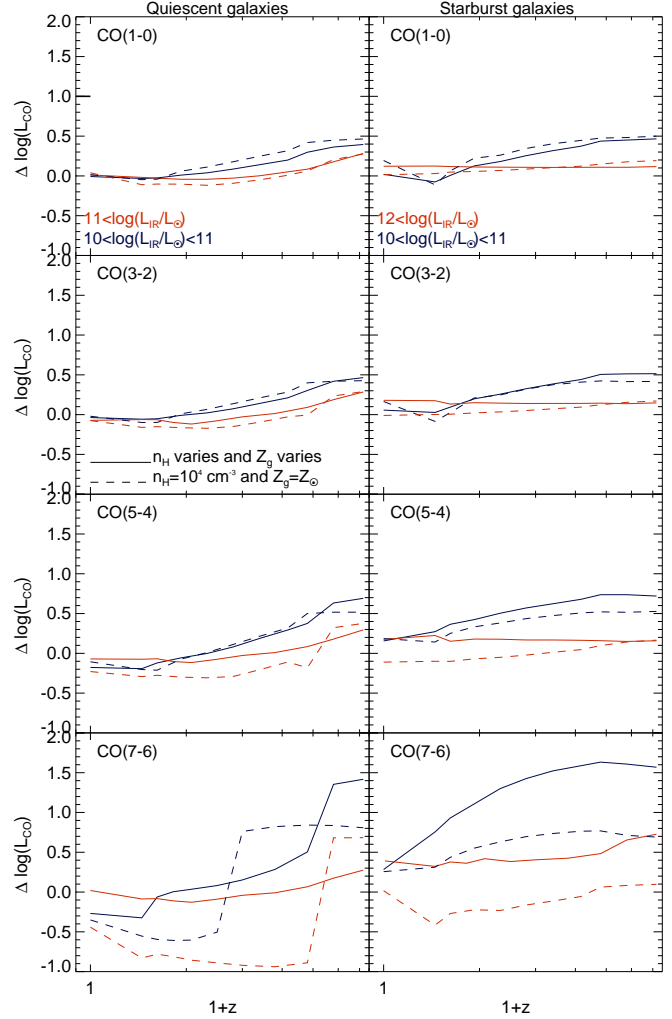


Figure 11. Logarithm of the median ratio between the predicted CO luminosity in the PDR model variants and the standard GALFORM+UCL_PDR model as a function of redshift for two alternative PDR models. Quiescent and starburst galaxies are shown in the left-hand and right-hand columns, respectively, and for four CO transitions, CO(1–0) (top panels), CO(3–2) (middle-top panels), CO(5–4) (middle-bottom panels) and CO(7–6) (bottom panels), and two IR luminosities ranges (blue and red, as labelled), which are different in the right and left-hand columns to enhance differences. The assumptions made in these two alternative PDR models are: (i) constant $n_H = 10^4 \text{ cm}^{-3}$ and metallicity, $Z_g = Z_\odot$ (dashed lines), and (ii) varying Z_g and n_H (solid lines).

$n_H \propto n_{H,\min} \propto G_{\text{UV}}$ on the predictions presented in §3 and §4. For this we select a subset of PDR models from Table 1, so that $n_H = 10^3 \text{ cm}^{-3} (G_{\text{UV}}/G_0)$. We repeat the analysis of §4 using this subset of PDR models. The ratio between the predicted CO luminosity in the standard GALFORM+UCL_PDR and the model using a variable n_H is shown in Fig. 11 as solid lines.

Allowing n_H to vary has a small impact on the predicted CO luminosities at low CO transitions typically less than a factor of 3, and gives slightly smaller differences with respect to the standard GALFORM+UCL_PDR model than the model which uses a $Z_g = Z_\odot$ and $n_H = 10^4 \text{ cm}^{-3}$ (dashed lines in Fig. 11). This suggests that including the gas metallicity information from GALFORM in the PDR has a similar impact on the predicted CO luminosities

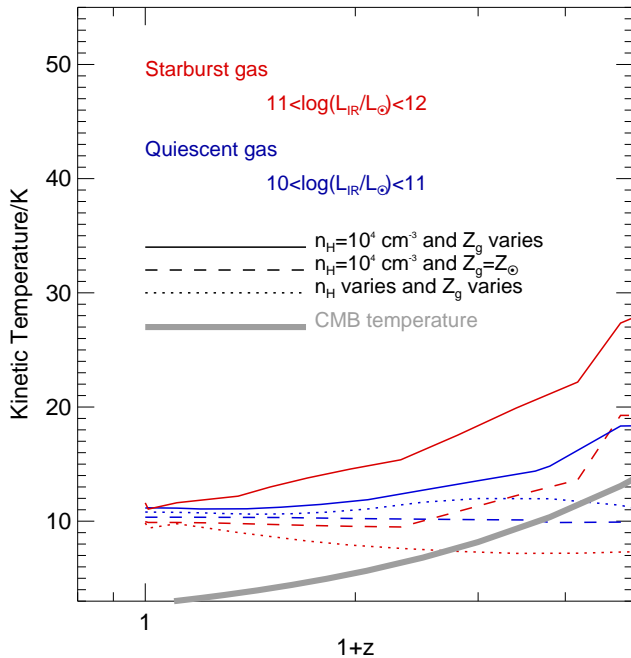


Figure 12. Kinetic temperature of the gas in molecular clouds for quiescent (blue curves) and starburst (red curves) gas phases in the ISM of galaxies as a function of redshift and for IR luminosities in the range $10^{10} - 10^{11} L_{\odot}$ for quiescent gas and $10^{11} - 10^{12} L_{\odot}$ for starburst gas. Lines show the median of the predicted T_K , for the two models of Fig. 11, in addition to the standard GALFORM+UCL-PDR model, which assumes $n_H = 10^4 \text{ cm}^{-3}$ and varying metallicity, as labelled. For reference, the Cosmic Microwave Background temperature is shown as a thick grey solid line. For the same line style, starbursts have higher T_K than quiescent gas in galaxies.

than the assumption of a constant $n_H = 10^4 \text{ cm}^{-3}$. This again supports our interpretation of the major role that metallicity plays in determining X_{CO} (Bayet et al. 2012, in prep.). When moving to high CO transitions, deviations from the CO luminosities predicted by the model with variable n_H become more important. There is a tendency to produce fainter (brighter) CO emission from high CO transitions at low (high) redshifts with respect to the standard model. This is because in the standard model there is a clear increase of temperature with redshift for both, quiescent and starburst gas, that is not as obvious in the case of the quiescent gas in the subset of PDR models in which n_H is varied (Fig. 12).

We have argued that metallicity plays an important role in determining the average transmission of UV photons in galaxies and that therefore affects the incident UV flux. This translates into low metallicity galaxies having higher temperatures. Fig. 12 shows the kinetic temperature evolution for the standard GALFORM+UCL-PDR model and the two subsets of PDR models we describe above for two ranges of IR luminosities. In the subset of PDR models where the metallicity is fixed, there is no visible evolution of T_K with redshift for quiescent gas. This supports our conclusion that the ISM metallicity evolution is a main driver of the increasing T_K with redshift in quiescent gas in the standard GALFORM+UCL-PDR model (§4.2.3). In the PDR subset of models where n_H varies, the trend between T_K and z for the quiescent gas is only weakly recovered at $z < 2.5$. In the case of starburst gas, the main driver of the trend of increasing T_K with redshift, is the increasing G_{UV} with redshift, that is only weakly affected by metallicity (see §4.2.3). Thus, the subset of PDRs with fixed metal-

licity recovers the trend of the standard GALFORM+UCL-PDR model. In the case of the subset of PDRs with variable n_H , the trend is lost due to the more efficient cooling in the PDR due to the higher n_H .

The small deviations in the emission of low CO transitions introduced by different assumptions in the PDR modelling suggest that the predictions presented in this paper for these transitions are robust under these changes. However, high CO transitions are more sensitive to the assumptions in the PDR modelling. The small number of observations available in these transitions does not so far allow us to distinguish these different possibilities. More data on these high CO transitions are needed, particularly if they cover a wide redshift range. Homogeneity in the observed samples, even though it is desired, is not essential given that our modelling permits the prediction of a plethora of galaxy properties, which allows us to select galaxies to have similar properties to the observed ones.

6 PREDICTIVE POWER OF THE GALFORM+UCL-PDR MODEL

We have shown that the predictions of the GALFORM+UCL-PDR model for CO emission are in good agreement with observations of galaxies in the local and high redshift Universe. Consequently, this coupled model is a powerful theoretical tool to study the observability of molecular lines in different types of galaxies and can therefore contribute to the development of science cases for the new generation of millimeter telescopes. In this section we focus on star-forming galaxies at high redshift, selected through two different techniques based on broad band colours: (i) BzK colour selection (Daddi et al. 2004), which can be used to select star-forming galaxies in the redshift range $1.4 \lesssim z \lesssim 2.5$, and (ii) the Lyman-break technique which is used to select star-forming galaxies at $z \sim 3 - 10$. In this section, we study the observability of these star-forming galaxies with ALMA. We use AB magnitudes throughout this section.

6.1 BzK galaxies

The BzK colour selection has shown to be efficient at selecting galaxies around $z \sim 2$ Daddi et al. (2004). BzK-selected galaxies have been used to study the build-up of the stellar mass, the SF history of the Universe and properties of star-forming and passive galaxies at the peak of SF activity (e.g. Daddi et al. 2005, 2007; Lin et al. 2011). The BzK criterion is based on observer frame magnitudes in the B , z and K bands. Star-forming galaxies, also referred to as sBzK, are selected as those whose BzK colour index $\text{BzK} = (z - K)_{\text{AB}} - (B - z)_{\text{AB}} > -0.2$.

The model predicts that the BzK criterion is a very efficient way to select star-forming galaxies; with only a small contamination of $\approx 10\%$ of galaxies outside the redshift range $1.4 < z < 2.5$. Furthermore, for a given limit m_K , there is a positive correlation between the BzK colour index and the SFR of galaxies, although with a large dispersion (Merson et al. 2012). Large BzK colour indices ($\text{BzK} > 1.5$) correspond almost exclusively to highly star-forming galaxies, $\text{SFR} \gtrsim 10 M_{\odot} \text{ yr}^{-1}$.

We take the galaxy population predicted by the GALFORM model at $z = 2$ and select a sample of sBzK galaxies based on their BzK colour indices and apparent K-band magnitudes: $\text{BzK} > -0.2$ and $m_K < 24$. The latter cut corresponds roughly to the deepest K-band surveys to date (Bielby et al. 2011). We randomly select four galaxies from this $z = 2$ BzK sample in bins of BzK colour index,

Table 2. Properties of the four star-forming BzK galaxies at $z = 2$: row (1) observer frame, extinguished K-band absolute magnitude, (2) BzK colour index, (3) molecular gas mass, (4) stellar mass, (5) SFR, (6) gas metallicity, (7) molecular gas half-mass radius, (8) line-of-sight CO velocity width, (9) velocity-integrated CO line flux of the CO(1 – 0), the (10) CO(3 – 2) and the (11) CO(6 – 5) emission lines, in (12), (13) and (14) the integration time to get a detection at the level indicated in the parenthesis in the band 1, band 3 and band 6 of ALMA for the CO(1 – 0), CO(3 – 2) and CO(6 – 5) emission lines, respectively. We used the full ALMA configuration (50 antennae) and average water vapor conditions (≈ 1.2 -1.5mm of column density) to simulate the observations of these galaxies. We also list the central frequency, ν_c , bandwidth, $\Delta\nu$, and angular resolution, R , used to simulate the observations.

Properties $z = 2$ sBzK	BzK+gal1	BzK+gal2	BzK+gal3	BzK+gal4
(1) $M_K - 5\log(h)$	-22.9	-21.3	-21.3	-21.5
(2) BzK index	0.23	0.95	1.2	1.52
(3) $\log(M_{\text{mol}}/M_{\odot})$	9.6	9.9	9.3	10.6
(4) $\log(M_{\text{stellar}}/M_{\odot})$	10.6	10.6	10.2	10.7
(5) $\text{SFR}/M_{\odot} \text{ yr}^{-1}$	3.7	3.72	1.0	19.3
(6) Z_{gas}/Z_{\odot}	0.63	1.15	1.33	1.4
(7) $r_{50}^{\text{mol}}/\text{kpc}$	0.8	2.0	2.8	1.9
(8) $\sigma_{\text{CO}}^{\text{los}}/\text{km s}^{-1}$	119	199	177	273
(9) $S_{\text{CO}(1-0),V}/\text{mJy km s}^{-1}$	16.95	8.7	2.4	46.38
(10) $S_{\text{CO}(3-2),V}/\text{mJy km s}^{-1}$	101.9	52.8	14.5	279.9
(11) $S_{\text{CO}(6-5),V}/\text{mJy km s}^{-1}$	12.7	8.1	2.2	42.8
(12) $\tau_{\text{int,band1}}(1-0) (1\sigma \text{ noise})$	3h (0.03mJy)	5.3d (0.0043mJy)	56d (0.00135mJy)	8.6h (0.017mJy)
(13) $\tau_{\text{int,band3}}(3-2) (1\sigma \text{ noise})$	21.6m (0.17mJy)	14.9h (0.027mJy)	4.3d (0.01mJy)	1h (0.1mJy)
(14) $\tau_{\text{int,band6}}(6-5) (1\sigma \text{ noise})$	4.8h (0.67Jy)	5.7d (0.004mJy)	53d (0.0013mJy)	8.7h (0.016mJy)
band configuration	ν_c	$\Delta\nu$	R/arcsec	
(15) band 1	38.3 GHz	0.05 GHz	4.8	
(16) band 3	115.27 GHz	0.11 GHz	1.48	
(17) band 6	230.49 GHz	0.2 GHz	0.67	

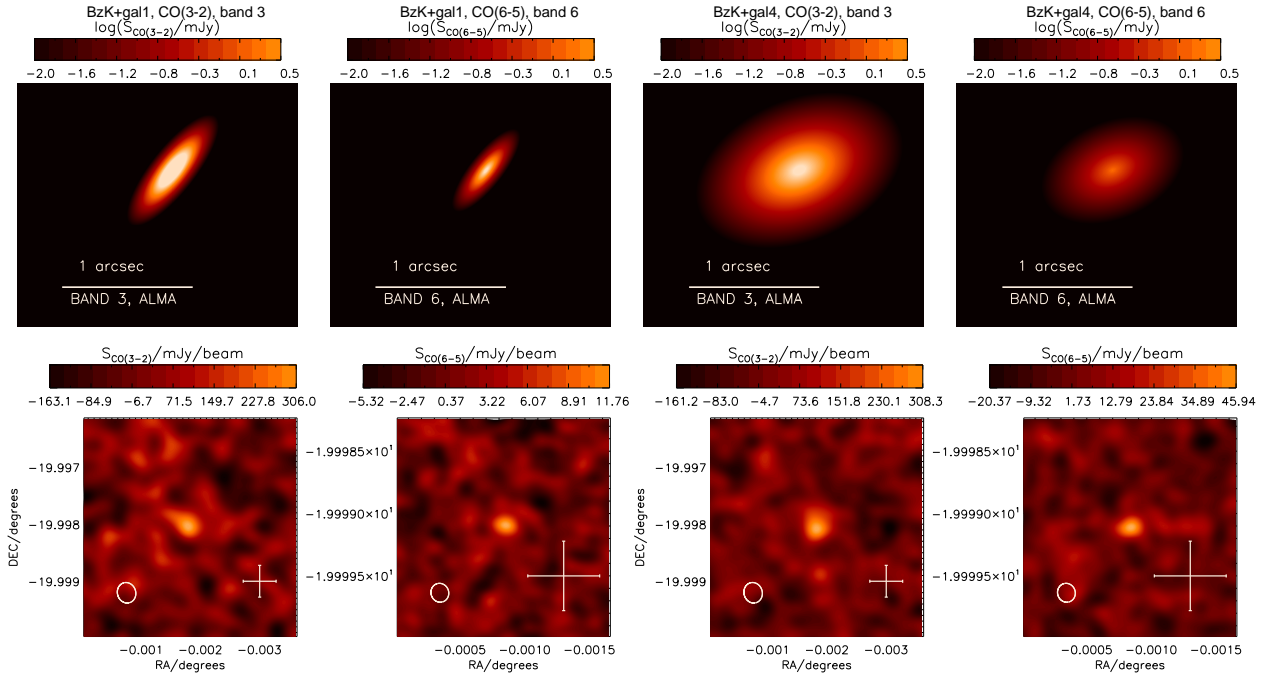


Figure 13. Two star-forming BzK galaxies at $z = 2$, BzK+gal1 (left-hand and middle-left panels) and BzK+gal4 (right-hand and middle-right panels). *Top panels:* the CO(3 – 2) (left panel) and CO(6 – 5) (right panel) flux maps in logarithmic units of mJy/pixel. Horizontal lines show 1 arcsec scale and the band in which the CO transition would be observed in ALMA at this redshift is labelled (band 3 and 6, for the CO(3 – 2) and CO(6 – 5), respectively). *Bottom panels:* the simulated observations of the CO(3 – 2) and CO(6 – 5) flux maps in declination vs. right ascension. Flux is in units of mJy/beam. Maps corresponds to the outputs of the CASA software, after convolving the original map with the primary beam and including an atmospheric model for the background noise, in the full ALMA configuration (50 antennae). Ellipses at the bottom-left corner indicate the beam size and shape and the cross shows $1 \times 1 \text{ arcsec}^2$. The flux scale is shown at the top of each panel. Some relevant properties of these galaxies are listed in Table 2, along with the integration time used to generate the CASA maps.

and list selected properties in Table 2. In Table 2, the CO line velocity width, $\sigma_{\text{CO}}^{\text{los}}$, corresponds to the line-of-sight circular velocity and the velocity dispersion in the case of the disk and the bulge components, respectively (considering a random inclination). We choose to focus on the CO(1–0), CO(3–2) and CO(6–5) emission of these galaxies, which fall into band 1, 3 and 6 of ALMA, respectively, but note that other CO lines also fall into the ALMA bands at this redshift.

We used the software CASA⁴, which is part of the observational tools associated with ALMA, to simulate observations of model galaxies, by including instrumental and atmospheric effects, such as the convolution with the primary beam and the sky noise. We calculate the integration times⁵ necessary to obtain a theoretical root mean square sensitivity of at least 5 times lower than the peak CO flux with the full ALMA configuration (50 antennae) under average water vapor conditions ($\approx 1.2 - 1.5$ mm of column density). The peak CO flux corresponds to $s_{\nu} = S_{\text{CO},\nu}/\sigma_{\text{los}}$. Input parameters used in the CASA software and integration times are listed in Table 2 for both CO emission lines considered.

Fig. 13 shows two of the four BzK galaxies listed in Table 2. For each of these galaxies we show mock images with perfect angular resolution and no noise (top panels) and the simulated observations (bottom panels) for the CO(3–2) and CO(6–5) lines assuming random inclinations and position angles. The beam of the instrument⁶ is plotted in the panels showing the simulated images. Note that the angular extents of the output images for the CO(3–2) and CO(6–5) observations are different: crosses in the panels show for reference 1×1 arcsec². This happens because the lower frequencies are observed with lower angular resolution than the higher frequencies. From the integration times calculated here, it is clear that ALMA can obtain 5σ detections in relatively short integration times only in some of these galaxies. Even though sBzKs of Table 2 have velocity-integrated CO fluxes that are large, these galaxies are sufficiently big so that the peak flux in some cases is faint enough to need large integration times. Note that, if the required 5σ detection is in the integrated flux instead of peak flux, the integration times are generally reduced to $\tau_{\text{int}} < 1$ hour.

This indicates that the sBzK selection could be an effective way of constructing a parent catalogue of galaxies to follow-up with ALMA⁷. However, spatially resolving the ISM of these high redshift galaxies will be a very difficult task because (1) high order CO lines can be observed at better angular resolution, but are at the same time fainter and therefore need much longer exposures (see Fig. 9), and (2) the decreasing galaxy size with increasing redshift predicted by GALFORM (Lacey et al. 2011) and observed by several authors (e.g. Bouwens et al. 2004; Oesch et al. 2010), imply that galaxies at these high redshifts are intrinsically smaller than their local universe counterparts, and therefore even more difficult to resolve.

In the examples of Fig. 13, it is possible to observe more than one CO emission line in reasonable integration times, which could help to constrain the excitation levels of the cold ISM in

these galaxies. Note that observationally, targeting of sBzK galaxies to study CO has been done by Daddi et al. (2010) for 5 very bright galaxies using the PdBI and integration times > 10 hours per source. Their CO emission is $\approx 2 - 3$ larger than our brightest example, BzK+gal4, which requires an integration time in ALMA of less than 20 minutes in CO(3–2), indicating again that ALMA will be able to detect CO routinely in these galaxies, even with the relatively modest amount of emission from the CO(3–2) transition.

6.2 Lyman-break galaxies

Lyman-break galaxies (LBGs) are star-forming galaxies which are identified through the Lyman-break feature in their spectral energy distributions. This feature is produced by absorption by neutral hydrogen in the atmospheres of massive stars, in the ISM of the galaxy and in the intergalactic medium (Steidel & Hamilton 1992; Steidel et al. 1996). Colour selection of these galaxies has been shown to be very efficient and has allowed the statistical assessment of their properties (such as the rest-frame UV LF and the size-luminosity relation; Steidel et al. 1996; Bouwens et al. 2004). LBGs are of great interest as a tracer of the galaxy population at high redshift (see Lacey et al. 2011). These galaxies are at even higher redshifts than BzK galaxies, and are therefore key to probing the evolution in the ISM of galaxies at early epochs. We show in the following subsection examples of LBGs at $z = 3$ and $z = 6$.

6.2.1 Lyman-break galaxies at $z = 3$

Fig. 14 shows four LBGs at $z = 3$ from the GALFORM+UCL-PDR model. In the top panels we show mock images of the CO(3–2) emission of the model LBGs, and in the bottom panels we show the simulated ALMA observations. The intrinsic properties of these four galaxies are listed in Table 3, along with other relevant information, as discussed below. Here, the rest-frame UV luminosity includes dust extinction. We estimate integration times as in §6.1 for imaging the CO(3–2), CO(5–4) and CO(6–5) transitions, modifying the inputs accordingly (e.g. ν_c , $\Delta\nu$, resolution). Integration times are also listed in Table 3 for the three CO emission lines. Note that the CO(6–5) transition in three of the four LBGs shown here needs integration times larger than a day to obtain a 5σ detection. These cases are not suitable for observation, but it is interesting to see how long an integration would be needed to be to get a minimum signal for a detection in such a high order CO transition. However, in the four LBGs it would be possible to observe more than one CO transition line, which would allow the physical conditions in the ISM in these galaxies to be constrained.

LBGs were randomly chosen from the full sample of LBGs at $z = 3$ in the GALFORM model, in bins of UV rest-frame luminosity. The break in the UV LF at $z = 3$ is at $M_{\text{UV}}^* - 5\log(h) \approx -20.3$ (Reddy & Steidel 2009), so the LBGs in Fig. 14 have a UV luminosities covering a large range around L_{UV}^* . In terms of the $M_{\text{stellar}} - \text{SFR}$ plane (see Lagos et al. 2011b), the four LBGs in Table 3 lie on the so-called ‘main’ sequence. The integration times we calculate for these galaxies indicate that imaging $z = 3$ LBGs will be an easy task for ALMA, detecting CO(3–2) in integrations shorter than few hours per source. Therefore LBG selection should provide a promising way of constructing a parent galaxy catalogue to follow up using ALMA. Note that imaging of the CO(3–2) line in these LBGs at $z = 3$ is easier than in the BzKs at $z = 2$ shown before. This happens because LBGs are predicted to typically have smaller σ_{los} than BzKs due to their lower baryonic content.

⁴ Specifically, we use the ALMA OST software developed by the ALMA regional centre in the UK, <http://almaost.jb.man.ac.uk/>.

⁵ Integration times were calculated using the ALMA sensitivity calculator <https://almascience.nrao.edu/call-for-proposals/sensitivity-calculator>.

⁶ The beam corresponds to the FWHM of a two-dimensional gaussian fitted to the central lobe of the Point Spread Function.

⁷ The ALMA basic specifications are described in <https://almascience.nrao.edu/about-alma/full-alma>

Table 3. Properties of the four Lyman-break galaxies at $z = 3$ plotted in Fig 14: row (1) rest-frame, extinguished UV magnitude, columns (2)-(7) are as in Table 2, (8) velocity-integrated CO line flux of the CO(3 – 2), the (9) CO(5 – 4), and (10) the CO(6 – 5) emission lines, (11), (12) and (13) show the integration times to get a detection at the sensitivity indicated in the parentheses in band 3, 4 and 5 of ALMA for the CO(3 – 2), CO(5 – 4) and CO(6 – 5) emission lines, respectively. We also list ν_c , $\Delta\nu$ and R used to simulate observations.

Properties $z = 3$ LBGs	LBG+gal1	LBG+gal2	LBG+gal3	LBG+gal4
(1) $M_{\text{rest}}(1500\text{\AA}) - 5\log(h)$	-18.4	-19.25	-20.46	-20.77
(2) $\log(M_{\text{mol}}/M_{\odot})$	9.6	9.7	9.9	9.93
(3) $\log(M_{\text{stellar}}/M_{\odot})$	8.3	9	9.6	9.8
(4) $\text{SFR}/M_{\odot} \text{ yr}^{-1}$	1.8	2.1	9.5	25.2
(5) Z_{gas}/Z_{\odot}	0.05	0.07	0.17	0.15
(6) $r_{50}^{\text{mol}}/\text{kpc}$	1.8	1.1	2.2	2.35
(7) $\sigma_{\text{CO}}^{\text{los}}/\text{km s}^{-1}$	73	58	66	103
(8) $S_{\text{CO}(3-2),V}/\text{mJy km s}^{-1}$	13.76	18.42	58.04	63
(9) $S_{\text{CO}(5-4),V}/\text{mJy km s}^{-1}$	9.7	12.97	41.2	72.6
(10) $S_{\text{CO}(6-5),V}/\text{mJy km s}^{-1}$	2.1	2.8	11.6	39.3
(11) $\tau_{\text{int,band3}}(3-2) (1\sigma \text{ noise})$	2.8h (0.038mJy)	1h (0.063mJy)	7.7m (0.18mJy)	7m (0.19mJy)
(12) $\tau_{\text{int,band4}}(5-4) (1\sigma \text{ noise})$	8.7h (0.026mJy)	3.1h (0.045mJy)	22.8m (0.127mJy)	8.1m (0.214mJy)
(13) $\tau_{\text{int,band5}}(6-5) (1\sigma \text{ noise})$	53d (0.0028mJy)	42d (0.0032mJy)	2.9d (0.012mJy)	9.4h (0.038mJy)
band configuration	ν_c	$\Delta\nu$	R/arcsec	
(14) band 3	86.45 GHz	0.1 GHz	1.48	
(15) band 4	143.7 GHz	0.09 GHz	1.07	
(16) band 5	172.5 GHz	0.11 GHz	0.89	

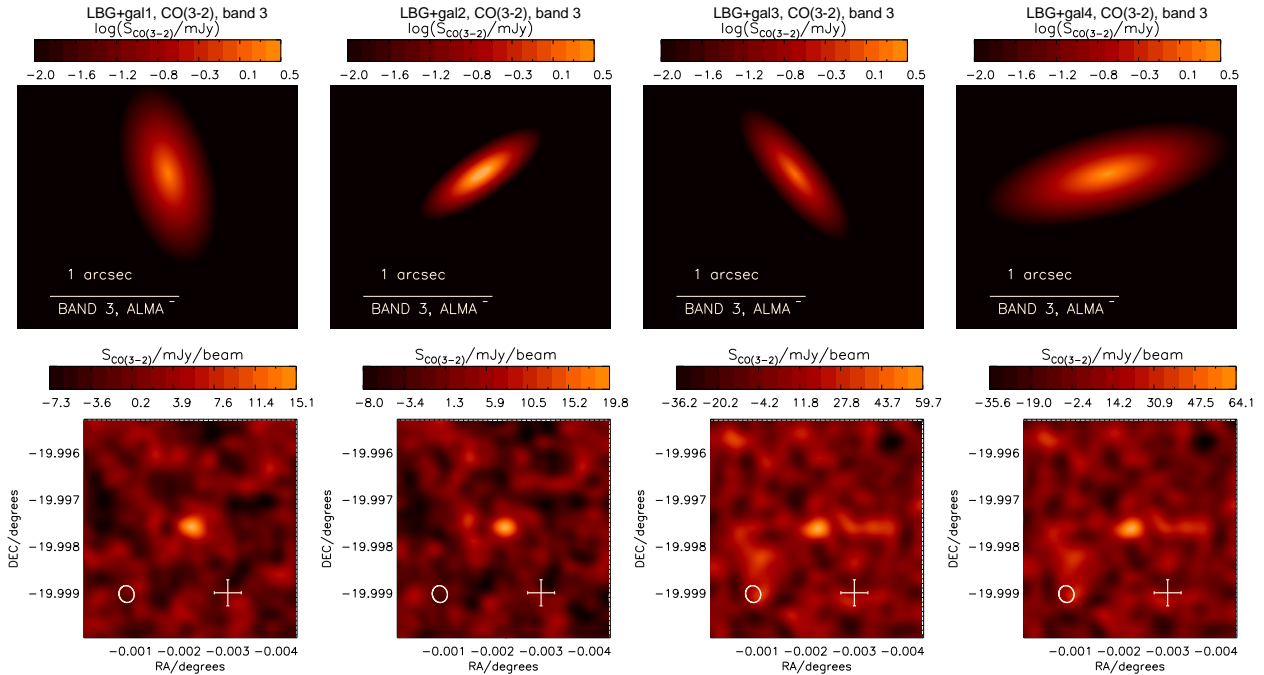


Figure 14. Four Lyman-break galaxies at $z = 3$. *Top panels:* the CO(3 – 2) flux maps in logarithmic units of mJy/beam. The horizontal line shows 1 arcsec. *Bottom panels:* the observed CO(3 – 2) flux maps in declination vs. right ascension. Flux is in units of mJy/beam. Maps corresponds to the outputs of the CASA software, after convolving the original map with the primary beam and including an atmospheric model for the background noise. Ellipses in the bottom-left corner indicate the beam size and shape and the cross indicates a $1 \times 1 \text{ arcsec}^2$. The flux scale is shown at the top of each figure. Some relevant properties of these galaxies are listed in Table 3, along with the integration time used to generate the CASA maps of the LBGs.

The GALFORM model predicts a weak correlation between the molecular mass and the UV luminosity, $M_{\text{mol}} \propto L_{\text{UV}}^{0.5}$, while the SFR and the gas metallicity have stronger correlations with the UV luminosity. Thus, most of the differences in the CO emission between LBGs in Fig. 14 result from the different ISM conditions

(e.g. gas metallicities, Σ_{SFR}), rather than molecular gas mass. In the case of LBG+gal4, the CO(5 – 4) flux is larger than that of CO(3 – 2). This happens because this LBG is undergoing a bright starburst, which leads to a much more excited ISM. Its CO SLED peaks at higher J and falls slowly as J increases, compared to the

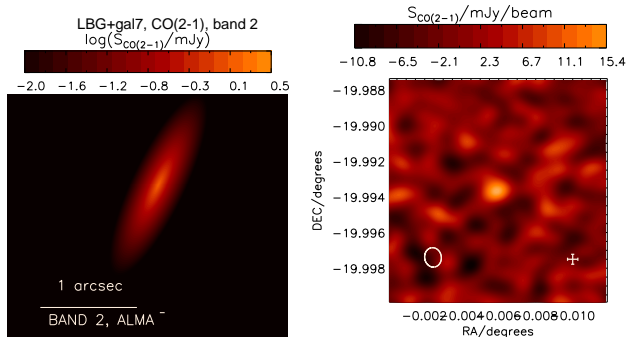


Figure 15. As in Fig. 14 but for a Lyman-break galaxies at $z = 6$. At this redshift we focus on the CO(2 – 1) emission line, which falls into the ALMA band 1. Some relevant properties of this galaxy are listed in Table 4 as LBG+gal7.

other LBGs shown here. These differences in the excitation levels of CO have a big impact on the observability of LBGs in the high-order CO transitions ($J > 5$), producing large variations in the integration times needed to get a $\gtrsim 5\sigma$ detection. However, it is important to remark that, in this model, starburst galaxies constitute only $\approx 10\%$ of the galaxies with $M_{UV} - 5\log(h) < -18$ at this redshift, even though their number density is much higher compared to low redshifts.

6.2.2 Lyman-break galaxies at $z = 6$

We select four Lyman-break model galaxies at $z = 6$ in terms of their UV luminosity. Given the intrinsically faint CO emission of these galaxies, we estimate the integration times for these $z = 6$ LBGs assuming good weather conditions (i.e. a water vapour column density of 0.5 mm), unlike BzKs and $z = 3$ LBGs, for which we assumed average weather conditions. Note that only two LBGs out of the four shown in Table 4 require an integration time to detect the CO(2 – 1) emission line of $\tau_{\text{int}} < 1$ day. We show one of these two ‘observable’ LBGs in Fig 15. At this very high redshift, the detection of any CO emission line will be a challenging task even for ALMA. Predictions from hydrodynamic simulations of $z = 6$ Lyman- α emitters reach a similar conclusion. Vallini et al. (2012), using a constant $X_{\text{CO}(1-0)}$ and assuming local thermodynamic equilibrium to estimate the luminosities of higher CO transitions showed that only the brightest Lyman- α emitters at $z = 6$ would be suitable for observation in the full ALMA configuration in under < 10 hours of integration time.

A possible solution for the study of these very high redshift galaxies is CO intensity mapping using instruments which are designed primarily to detect atomic hydrogen, such as the South-African SKA pathfinder, MeerKAT⁸, and in the future, the Square Kilometer Array⁹ (SKA). At such high redshifts these telescopes will also cover the redshifted frequencies of low- J CO transitions. Given their larger field-of-view compared to ALMA, it is possible to collect the molecular emission of all galaxies in a solid angle and to isolate the emission from a narrow redshift range by cross-correlating emission maps of different molecules. From this, it is possible to construct the emission line power spectrum and its evolution, inferring valuable information, such as the total molecular

content from galaxies that are too faint to be detected individually (Visbal et al. 2010, 2011; see Pritchard & Loeb 2011 for a review).

7 DISCUSSION AND CONCLUSIONS

We have presented a new theoretical tool to study the CO emission of galaxies and its connection to other galaxy properties. One of the aims of this work is to expand the predictive power of galaxy formation models. Previously, there was no connection between the conditions in the ISM in model galaxies and their CO emission. The CO emission from a galaxy was obtained from the predicted mass of molecular hydrogen essentially by adopting an ad-hoc X_{CO} . In this new hybrid model, the value of X_{CO} is computed by the PDR model after taking as inputs selected predicted galaxy properties. A lack of resolution and the use of simplifying assumptions (which make the calculation tractable) means that we use proxy properties to describe the conditions in the ISM. At the end of this exercise, the number of testable predictions which can be used to reduce the model parameter space has been considerably increased (e.g. CO luminosity functions, CO-to-IR luminosity ratios and CO SLEDs).

The hybrid model presented in this work combines the galaxy formation model GALFORM with the Photon Dominated Region code UCL-PDR, which calculates the chemistry of the cold ISM. We use state-of-the-art models: the Lagos et al. (2011a) galaxy formation model, which includes a calculation of the H_2 abundance in the ISM of galaxies and self-consistently estimates the instantaneous SFR from the H_2 surface density, and the Bayet et al. (2011) PDR model, which models the thermal and chemical states of the ISM in galaxies. The combined code uses the molecular gas mass of galaxies and their average ISM properties as predicted by GALFORM as inputs to the UCL-PDR model, to estimate the CO emission in several CO transitions for each galaxy. The average ISM properties required from GALFORM are the gas metallicity, and the average UV and X-ray radiation fields within galaxies. The gas metallicity and the X-ray luminosity from AGN are calculated directly in GALFORM. We use a phenomenological approach to estimate the UV radiation field by assuming a semi-infinite slab and a relation between the UV intensity and the SFR surface density in galaxies, with and without a correction for the average attenuation of UV photons. Given that the GALFORM model does not produce detailed radial profiles of galaxies, the combined GALFORM+UCL-PDR model focuses on the interpretation of global CO luminosities and their relation to other galaxy properties.

We show that this hybrid model is able to explain a wide range of the available CO observations of galaxies from $z = 0$ to $z = 6$, including LIRGs, ULIRGs, high redshift normal star-forming galaxies, SMGs and QSOs. Our main conclusion are:

(i) The GALFORM+UCL-PDR model predicts a $z = 0$ CO(1 – 0) luminosity function and CO(1 – 0)-to-IR luminosity relation in good agreement with observations (e.g. Keres et al. 2003; Solomon & Vanden Bout 2005). The model favours the inclusion of the attenuation of UV photons due to dust extinction in the estimate of the internal UV radiation field.

(ii) Starburst galaxies have lower CO(1 – 0)/IR luminosity ratios than normal star-forming galaxies, which leads to an anti-correlation between CO(1 – 0)/IR luminosity ratio and IR luminosity. This is due in part to the different SF laws in bursts compared to quiescent SF.

(iii) The GALFORM+UCL-PDR model predicts that the CO-to-IR luminosity ratio evolves weakly with redshift, regardless of

⁸ <http://www.ska.ac.za/meerkat/>

⁹ <http://www.skatelescope.org/>

Table 4. Properties of the four Lyman-break galaxies studied at $z = 6$. Properties are as in Table 3, but at this redshift, the lowest CO transitions that fall into ALMA bands are CO(6 – 5) and CO(7 – 6), at frequencies $\nu_{6-5}^{\text{obs}} = 98.8$ GHz and $\nu_{7-6}^{\text{obs}} = 115.2$ GHz, respectively.

Properties $z = 6$ LBGs	LBG+gal5	LBG+gal6	LBG+gal7	LBG+gal8
(1) $M_{\text{rest}}(1500\text{\AA}) - 5\log(h)$	-19.45	-19.6	-20.3	-20.9
(2) $\log(M_{\text{mol}}/M_{\odot})$	9.1	9.7	10	9.9
(3) $\log(M_{\text{stellar}}/M_{\odot})$	7.7	8.0	8.95	9.2
(4) $\text{SFR}/M_{\odot} \text{ yr}^{-1}$	6	2.9	6.3	3
(5) Z_{gas}/Z_{\odot}	0.03	0.05	0.1	0.3
(6) $r_{50}^{\text{mol}}/\text{kpc}$	0.27	1.1	2.1	0.5
(7) $\sigma_{\text{CO}}^{\text{los}}/\text{km s}^{-1}$	104	59	58	270
(8) $S_{\text{CO}(2-1), \text{V}}/\text{mJy km s}^{-1}$	3	4.067	16.93	5.69
(9) $S_{\text{CO}(6-5), \text{V}}/\text{mJy km s}^{-1}$	4.5	1.04	3.5	1.5
(10) $\tau_{\text{int, band1}(2-1) (1\sigma \text{ noise})$	3d (0.0057mJy)	12.7h (0.014mJy)	43m (0.057mJy)	2.9d (0.0058mJy)
(11) $\tau_{\text{int, band3}(6-5) (1\sigma \text{ noise})$	179d (0.0009mJy)	11d (0.0035mJy)	1d (0.012mJy)	101d (0.0011mJy)
band configuration	ν_c	$\Delta\nu$	R/arcsec	
(13) band 2	32.86 GHz	0.05 GHz	4.7	
(14) band 3	98.57 GHz	0.1 GHz	1.78	

the CO transition, and in agreement with local and high redshift observational data.

(iv) We find that the model is able to explain the shape and normalization of the CO SLEDs for local Universe LIRGs and high redshift SMGs. The model predicts a peak in their CO SLEDs, on average, at $J = 4$ and $J = 5$, respectively. The model predicts that the peak shifts to higher- J values with increasing IR luminosity. At a fixed IR luminosity, high redshift galaxies are predicted to have ISMs with higher gas kinetic temperature than low redshift galaxies, a result driven by the lower metallicities and higher SFR surface densities in such objects. The presence of an AGN affects the emission of high CO transitions in galaxies, with galaxies with AGN showing larger CO($J \rightarrow J-1$)/IR luminosity ratios at $J > 6$ than galaxies without AGN. The model predicts that observations of these high- J CO transitions should provide useful constraints on the heating effects of AGN on the ISM of galaxies.

We have shown that, despite its simplicity, this exploratory hybrid model is able to explain the observed CO emission of a wide range of galaxy types at low and high redshifts without the need for further tuning. This is the first time that a galaxy formation model has been able to successfully reproduce such a wide range of observations of CO along with other galaxy properties. This hybrid model can be used to predict the observability of galaxies with the current and upcoming generation of millimeter telescopes, such as LMT, GMT, PdBI and ALMA. This is also applies to radio telescopes which can be used to study molecular emission of high redshift galaxies, such as MeerKAT, and further into the future, the SKA.

As an example of the diagnostic power of the GALFORM+UCL-PDR model, we study the observability of high redshift star-forming galaxies with ALMA, which is one of its key science goals. In particular, we focus on colour-selected BzK galaxies at $z = 2$ and LBGs at $z = 3$ and $z = 6$. We use the ALMA OST software to simulate observations of the GALFORM+UCL-PDR model galaxies. For the first time, we present the expected CO fluxes and the integration times needed to obtain a 5σ detections in the full ALMA configuration. We find that ALMA should be able to observe star-forming galaxies in low- J CO transitions routinely up to $z \approx 3$, with integration times

of less than a few hours per source, and in a large fraction of the samples, in under 1 hour. However, for star-forming galaxies at $z = 6$, this will be a much more difficult task, given their lower gas masses and metallicities, which lead to lower CO luminosities. For these galaxies, future radio telescopes offer a promising alternative of intensity mapping of molecular emission lines, from which it is possible to learn about the molecular content of faint galaxies. Therefore, colour selection of galaxies should be an effective way to construct parent samples for follow up with ALMA.

Further observational data on the CO SLEDs of galaxies and how these relate to other galaxy properties will be key to constraining the physical mechanisms included in the model, and determine whether our model is sufficient to explain the observations (particularly of high-redshift galaxies), or whether an improved (more general) calculation is needed, or indeed if further physical processes have to be considered. The physics included and the simplifications made in this work seem to be good enough to explain current observations of CO. The GALFORM+UCL-PDR model will facilitate the interpretation of observations which aim to studying the evolution of the mass of molecular gas in galaxies and assist the planning of science cases for the new generation of millimeter telescopes, and lays the foundation for a new generation of theoretical models.

ACKNOWLEDGEMENTS

We thank Serena Viti, Ian Smail, Mark Swinbank, Linda Tacconi, Karin Sandstrom and Desika Narayanan for useful discussion and comments on this work. We thank the anonymous referee for helpful suggestions that improved this work. We thank the ALMA OT team, and particularly Adam Avinson, Justo González and Rodrigo Tobar, for helpful remarks on the ALMA OT and the CASA software. CL gratefully acknowledges a STFC Gemini studentship. EB acknowledges the rolling grants ‘Astrophysics at Oxford’ PP/EE/E001114/1 and ST/H504862/1 from the UK Research Councils and the John Fell OUP Research fund, ref 092/267. JEG is supported by a Banting Fellowship, administered by the Natural Science and Engineering Council of Canada. The authors benefited from a visit of EB to Durham University supported by a STFC

visitor grant at Durham. Calculations for this paper were mainly performed on the ICC Cosmology Machine, which is part of the DiRAC Facility jointly funded by STFC, the Large Facilities Capital Fund of BIS, and Durham University.

REFERENCES

- Aravena M., Carilli C. L., Salvato M., Tanaka M., Lentati L., Schinnerer E., Walter F., Riechers D. et al, 2012, *ApJ* in press, ArXiv:1207.2795
- Asplund M., Grevesse N., Sauval A. J., 2005, in *Astronomical Society of the Pacific Conference Series*, Vol. 336, *Cosmic Abundances as Records of Stellar Evolution and Nucleosynthesis*, T. G. Barnes III & F. N. Bash, ed., pp. 25–+
- Baugh C. M., 2006, *Reports on Progress in Physics*, 69, 3101
- Baugh C. M., Lacey C. G., Frenk C. S., Granato G. L., Silva L., Bressan A., Benson A. J., Cole S., 2005, *MNRAS*, 356, 1191
- Bayet E., Gerin M., Phillips T. G., Contursi A., 2009a, *MNRAS*, 399, 264
- Bayet E., Viti S., Williams D. A., Rawlings J. M. C., Bell T., 2009b, *ApJ*, 696, 1466
- Bayet E., Williams D. A., Hartquist T. W., Viti S., 2011, *MNRAS*, 414, 1583
- Bell T. A., Roueff E., Viti S., Williams D. A., 2006, *MNRAS*, 371, 1865
- Bell T. A., Viti S., Williams D. A., 2007, *MNRAS*, 378, 983
- Benson A. J., 2010, *Phys. Rep.*, 495, 33
- Bertram T., Eckart A., Fischer S., Zuther J., Straubmeier C., Wisotzki L., Krips M., 2007, *A&A*, 470, 571
- Bielby R., Hudelot P., McCracken H. J., Ilbert O., Daddi E., Le Fèvre O., Gonzalez-Perez V., Kneib J.-P. et al, 2011, ArXiv:1111.6997
- Bigiel F., Leroy A., Walter F., Brinks E., de Blok W. J. G., Madore B., Thornley M. D., 2008, *AJ*, 136, 2846
- Bigiel F., Leroy A. K., Walter F., Brinks E., de Blok W. J. G., Kramer C., Rix H. W., Schruba A. et al, 2011, *ApJ*, 730, L13+
- Blitz L., Fukui Y., Kawamura A., Leroy A., Mizuno N., Rosolowsky E., 2007, *Protostars and Planets V*, 81
- Blitz L., Rosolowsky E., 2006, *ApJ*, 650, 933
- Bolatto A. D., Leroy A. K., Jameson K., Ostriker E., Gordon K., Lawton B., Stanimirović S., Israel F. P. et al, 2011, *ApJ*, 741, 12
- Bonatto C., Bica E., 2011, *MNRAS*, 415, 2827
- Boselli A., Lequeux J., Gavazzi G., 2002, *A&A*, 384, 33
- Bothwell M. S., Chapman S. C., Tacconi L., Smail I., Ivison R. J., Casey C. M., Bertoldi F., Beswick R. et al, 2010, *MNRAS*, 405, 219
- Bothwell M. S., Kennicutt R. C., Lee J. C., 2009, *MNRAS*, 400, 154
- Bothwell M. S., Smail I., Chapman S. C., Genzel R., Ivison R. J., Tacconi L. J., Alaghband-Zadeh S., Bertoldi F. et al, 2012, ArXiv:1205.1511
- Bournaud F., Elmegreen B. G., Teyssier R., Block D. L., Puerari I., 2010, *MNRAS*, 409, 1088
- Bouwens R. J., Illingworth G. D., Blakeslee J. P., Broadhurst T. J., Franx M., 2004, *ApJ*, 611, L1
- Bower R. G., Benson A. J., Malbon R., Helly J. C., Frenk C. S., Baugh C. M., Cole S., Lacey C. G., 2006, *MNRAS*, 370, 645
- Casey C. M., Chapman S. C., Daddi E., Dannerbauer H., Pope A., Scott D., Bertoldi F., Beswick R. J. et al, 2009, *MNRAS*, 400, 670
- Chang R.-X., Shu C.-G., Hou J.-L., 2002, *Chin. Journ. Astronomy & Astrophysics*, 2, 226
- Cole S., Lacey C. G., Baugh C. M., Frenk C. S., 2000, *MNRAS*, 319, 168
- Combes F., García-Burillo S., Braine J., Schinnerer E., Walter F., Colina L., 2011, *A&A*, 528, 124
- Contini T., Treyer M. A., Sullivan M., Ellis R. S., 2002, *MNRAS*, 330, 75
- Cook M., Evoli C., Barausse E., Granato G. L., Lapi A., 2010, *MNRAS*, 402, 941
- Daddi E., Bournaud F., Walter F., Dannerbauer H., Carilli C. L., Dickinson M., Elbaz D., Morrison G. E. et al, 2010, *ApJ*, 713, 686
- Daddi E., Cimatti A., Renzini A., Fontana A., Mignoli M., Pozzetti L., Tozzi P., Zamorani G., 2004, *ApJ*, 617, 746
- Daddi E., Dickinson M., Morrison G., Chary R., Cimatti A., Elbaz D., Frayer D., Renzini A. et al, 2007, *ApJ*, 670, 156
- Daddi E., Renzini A., Pirzkal N., Cimatti A., Malhotra S., Stiavelli M., Xu C., Pasquali A. et al, 2005, *ApJ*, 626, 680
- Danielson A. L. R., Swinbank A. M., Smail I., Cox P., Edge A. C., Weiss A., Harris A. I., Baker A. J. et al, 2010, *MNRAS*, 1565
- de Jong R. S., 1996, *A&A*, 313, 377
- Dutton A. A., van den Bosch F. C., Dekel A., 2010, *MNRAS*, 405, 1690
- Engel H., Tacconi L. J., Davies R. I., Neri R., Smail I., Chapman S. C., Genzel R., Cox P. et al, 2010, *ApJ*, 724, 233
- Evans A. S., Solomon P. M., Tacconi L. J., Vavilkin T., Downes D., 2006, *AJ*, 132, 2398
- Fanidakis N., Baugh C. M., Benson A. J., Bower R. G., Cole S., Done C., Frenk C. S., 2011, *MNRAS*, 410, 53
- Fanidakis N., Baugh C. M., Benson A. J., Bower R. G., Cole S., Done C., Frenk C. S., Hickox R. C. et al, 2012, *MNRAS*, 419, 2797
- Feldmann R., Gnedin N. Y., Kravtsov A. V., 2012, *ApJ*, 747, 124
- Frayer D. T., Ivison R. J., Scoville N. Z., Evans A. S., Yun M. S., Smail I., Barger A. J., Blain A. W. et al, 1999, *ApJ*, 514, L13
- Frayer D. T., Ivison R. J., Scoville N. Z., Yun M., Evans A. S., Smail I., Blain A. W., Kneib J.-P., 1998, *ApJ*, 506, L7
- Fu J., Guo Q., Kauffmann G., Krumholz M. R., 2010, *MNRAS*, 409, 515
- Geach J. E., Smail I., Moran S. M., MacArthur L. A., Lagos C. d. P., Edge A. C., 2011, *ApJ*, 730, L19+
- Genzel R., Tacconi L. J., Gracia-Carpio J., Sternberg A., Cooper M. C., Shapiro K., Bolatto A., Bouché N. et al, 2010, *MNRAS*, 407, 2091
- Gnedin N. Y., Tassis K., Kravtsov A. V., 2009, *ApJ*, 697, 55
- González J. E., Lacey C. G., Baugh C. M., Frenk C. S., 2011, *MNRAS*, 413, 749
- Granato G. L., Lacey C. G., Silva L., Bressan A., Baugh C. M., Cole S., Frenk C. S., 2000, *ApJ*, 542, 710
- Grenier I. A., Casandjian J.-M., Terrier R., 2005, *Science*, 307, 1292
- Greve T. R., Bertoldi F., Smail I., Neri R., Chapman S. C., Blain A. W., Ivison R. J., Genzel R. et al, 2005, *MNRAS*, 359, 1165
- Henry R. B. C., Worthey G., 1999, *PASP*, 111, 919
- Hitschfeld M., Aravena M., Kramer C., Bertoldi F., Stutzki J., Bensch F., Bronfman L., Cubick M. et al, 2008, *A&A*, 479, 75
- Ivison R. J., Papadopoulos P. P., Smail I., Greve T. R., Thomson A. P., Xilouris E. M., Chapman S. C., 2011, *MNRAS*, 46
- Kauffmann G., Li C., Fu J., Saintonge A., Catinella B., Tacconi L. J., Kramer C., Genzel R. et al, 2012, *MNRAS*, 2601
- Kennicutt Jr. R. C., 1998, *ApJ*, 498, 541

- Kennicutt Jr. R. C., Bresolin F., Garnett D. R., 2003, *ApJ*, 591, 801
- Keres D., Yun M. S., Young J. S., 2003, *ApJ*, 582, 659
- Krumholz M. R., McKee C. F., Tumlinson J., 2009a, *ApJ*, 693, 216
- , 2009b, *ApJ*, 699, 850
- Lacey C. G., Baugh C. M., Frenk C. S., 2012. In preparation
- Lacey C. G., Baugh C. M., Frenk C. S., Benson A. J., 2011, *MNRAS*, 45
- Lacey C. G., Baugh C. M., Frenk C. S., Silva L., Granato G. L., Bressan A., 2008, *MNRAS*, 385, 1155
- Lagos C. D. P., Baugh C. M., Lacey C. G., Benson A. J., Kim H.-S., Power C., 2011a, *MNRAS*, 418, 1649
- Lagos C. D. P., Lacey C. G., Baugh C. M., Bower R. G., Benson A. J., 2011b, *MNRAS*, 416, 1566
- Lamareille F., Mouhcine M., Contini T., Lewis I., Maddox S., 2004, *MNRAS*, 350, 396
- Lara-López M. A., Cepa J., Bongiovanni A., Pérez García A. M., Ederoclite A., Castañeda H., Fernández Lorenzo M., Pović M. et al, 2010, *A&A*, 521, L53
- Leroy A., Bolatto A., Stanimirovic S., Mizuno N., Israel F., Bot C., 2007, *ApJ*, 658, 1027
- Leroy A. K., Bolatto A., Gordon K., Sandstrom K., Gratier P., Rosolowsky E., Engelbracht C. W., Mizuno N. et al, 2011, *ApJ*, 737, 12
- Leroy A. K., Walter F., Brinks E., Bigiel F., de Blok W. J. G., Madore B., Thornley M. D., 2008, *AJ*, 136, 2782
- Lin L., Dickinson M., Jian H.-Y., Merson A. I., Baugh C. M., Scott D., Foucaud S., Wang W.-H. et al, 2011, *ArXiv:1111.2135*
- Lisenfeld U., Espada D., Verdes-Montenegro L., Kuno N., Leon S., Sabater J., Sato N., Sulentic J. et al, 2011, *A&A*, 534, A102
- Mac Low M.-M., Glover S. C. O., 2012, *ApJ*, 746, 135
- Magdis G. E., Daddi E., Elbaz D., Sargent M., Dickinson M., Dannerbauer H., Aussel H., Walter F. et al, 2011, *ApJ*, 740, L15
- Mannucci F., Cresci G., Maiolino R., Marconi A., Gnerucci A., 2010, *MNRAS*, 408, 2115
- Marconi A., Risaliti G., Gilli R., Hunt L. K., Maiolino R., Salvati M., 2004, *MNRAS*, 351, 169
- Meijerink R., Spaans M., Israel F. P., 2007, *A&A*, 461, 793
- Meijerink R., Spaans M., Loenen A. F., van der Werf P. P., 2011, *A&A*, 525, A119
- Melbourne J., Salzer J. J., 2002, *AJ*, 123, 2302
- Merson A. I., Baugh C. M., Helly J. C., Gonzalez-Perez V., Cole S., Bielby R., Norberg P., Frenk C. S. et al, 2012, *ArXiv:1206.4049*
- Nagy Z., van der Tak F. F. S., Fuller G. A., Spaans M., Plume R., 2012, *A&A*, 542, A6
- Narayanan D., Cox T. J., Hayward C. C., Younger J. D., Hernquist L., 2009, *MNRAS*, 400, 1919
- Narayanan D., Groppi C. E., Kulesa C. A., Walker C. K., 2005, *ApJ*, 630, 269
- Narayanan D., Krumholz M. R., Ostriker E. C., Hernquist L., 2012, *MNRAS*, 421, 3127
- Neri R., Genzel R., Ivison R. J., Bertoldi F., Blain A. W., Chapman S. C., Cox P., Greve T. R. et al, 2003, *ApJ*, 597, L113
- Obreschkow D., Heywood I., Klöckner H.-R., Rawlings S., 2009, *ApJ*, 702, 1321
- Oesch P. A., Bouwens R. J., Carollo C. M., Illingworth G. D., Trenti M., Stiavelli M., Magee D., Labbé I. et al, 2010, *ApJ*, 709, L21
- Papadopoulos P. P., 2010, *ApJ*, 720, 226
- Papadopoulos P. P., van der Werf P., Xilouris E. M., Isaak K. G., Gao Y., Muehle S., 2011, *MNRAS* in press, *ArXiv:1109.4176*
- Peletier R. F., Davies R. L., Illingworth G. D., Davis L. E., Cawson M., 1990, *AJ*, 100, 1091
- Pelupessy F. I., Papadopoulos P. P., 2009, *ApJ*, 707, 954
- Pelupessy F. I., Papadopoulos P. P., van der Werf P., 2006, *ApJ*, 645, 1024
- Pritchard J. R., Loeb A., 2011, *ArXiv:1109.6012*
- Rahman N., Bolatto A. D., Xue R., Wong T., Leroy A. K., Walter F., Bigiel F., Rosolowsky E. et al, 2012, *ApJ*, 745, 183
- Reach W. T., Koo B.-C., Heiles C., 1994, *ApJ*, 429, 672
- Reddy N. A., Steidel C. C., 2009, *ApJ*, 692, 778
- Riechers D. A., 2011, *ApJ*, 730, 108
- Röllig M., Abel N. P., Bell T., Bensch F., Black J., Ferland G. J., Jonkheid B., Kamp I. et al, 2007, *A&A*, 467, 187
- Saintonge A., Kauffmann G., Kramer C., Tacconi L. J., Buchbender C., Catinella B., Fabello S., Graciá-Carpio J. et al, 2011, *MNRAS*, 415, 32
- Schruba A., Leroy A. K., Walter F., Bigiel F., Brinks E., de Blok W. J. G., Dumas G., Kramer C. et al, 2011, *AJ*, 142, 37
- Scoville N. Z., Frayer D. T., Schinnerer E., Christopher M., 2003, *ApJ*, 585, L105
- Sheth K., Blain A. W., Kneib J.-P., Frayer D. T., van der Werf P. P., Knudsen K. K., 2004, *ApJ*, 614, L5
- Silva L., Granato G. L., Bressan A., Danese L., 1998, *ApJ*, 509, 103
- Solomon P. M., Downes D., Radford S. J. E., Barrett J. W., 1997, *ApJ*, 478, 144
- Solomon P. M., Vanden Bout P. A., 2005, *ARA&A*, 43, 677
- Springel V., White S. D. M., Jenkins A., Frenk C. S., Yoshida N., Gao L., Navarro J., Thacker R. et al, 2005, *Nature*, 435, 629
- Steidel C. C., Giallisco M., Pettini M., Dickinson M., Adelberger K. L., 1996, *ApJ*, 462, L17
- Steidel C. C., Hamilton D., 1992, *AJ*, 104, 941
- Tacconi L. J., Genzel R., Neri R., Cox P., Cooper M. C., Shapiro K., Bolatto A., Bouché N. et al, 2010, *Nature*, 463, 781
- Tacconi L. J., Neri R., Chapman S. C., Genzel R., Smail I., Ivison R. J., Bertoldi F., Blain A. et al, 2006, *ApJ*, 640, 228
- Tremonti C. A., Heckman T. M., Kauffmann G., Brinchmann J., Charlot S., White S. D. M., Seibert M., Peng E. W. et al, 2004, *ApJ*, 613, 898
- Vallini L., Dayal P., Ferrara A., 2012, *MNRAS*, 2445
- van der Werf P. P., Berciano Alba A., Spaans M., Loenen E., Meijerink R., Riechers D., Cox P., Weiss A. et al, 2011, *ArXiv:1106.4825*
- van der Werf P. P., Isaak K. G., Meijerink R., Spaans M., Rykala A., Fulton T., Loenen A. F., Walter F. et al, 2010, *A&A*, 518, L42+
- Visbal E., Loeb A., 2010, *J. Cosmol. Astropart. Phys.*, 11, 16
- Visbal E., Trac H., Loeb A., 2011, *J. Cosmol. Astropart. Phys.*, 8, 10
- Weiß A., Downes D., Neri R., Walter F., Henkel C., Wilner D. J., Wagg J., Wiklind T., 2007, *A&A*, 467, 955
- Weiß A., Downes D., Walter F., Henkel C., 2005, *A&A*, 440, L45
- Wolfire M. G., Hollenbach D., McKee C. F., 2010, *ApJ*, 716, 1191
- Wolfire M. G., McKee C. F., Hollenbach D., Tielens A. G. G. M., 2003, *ApJ*, 587, 278
- Wong T., Blitz L., 2002, *ApJ*, 569, 157
- Yao L., Seaquist E. R., Kuno N., Dunne L., 2003, *ApJ*, 588, 771
- Young J. S., Scoville N. Z., 1991, *ARA&A*, 29, 581

APPENDIX A: THE CO LINE AND IR LUMINOSITY

In this appendix we explain in more detail how we calculate CO luminosities in the different units used in the paper and also the total IR luminosity.

We express the CO luminosity in three different ways: (i) as a line luminosity, L_{CO} , typically expressed in solar luminosities, (ii) as a velocity-integrated CO luminosity, $L_{\text{CO,V}}$, which is typically expressed in units of $\text{Jy km s}^{-1} \text{Mpc}^{-2}$, and (iii) as a brightness temperature luminosity, L'_{CO} , in units of $\text{K km s}^{-1} \text{pc}^{-2}$. We estimate these luminosities from the molecular hydrogen mass and the value of X_{CO} for each galaxy.

The spectral energy distribution of a source is characterised by the monochromatic luminosity, $l_\nu(\nu_{\text{rest}})$, where ν_{rest} is the rest-frame frequency. The total luminosity of the emission line we are interested in is simply the integral of $l_\nu(\nu_{\text{rest}})$ over the frequency width of the line,

$$L_{\text{CO}} = \int l_\nu(\nu_{\text{rest}}) d\nu_{\text{rest}}. \quad (\text{A1})$$

The units of L_{CO} are proportional to erg s^{-1} . Observationally, what is measured is the monochromatic flux, $s_\nu(\nu_{\text{obs}})$, where $\nu_{\text{obs}} = \nu_{\text{rest}}/(1+z)$ is the observed frequency. The flux density of this emitter is simply the frequency-integrated flux, $S = \int s_\nu(\nu_{\text{obs}}) d\nu_{\text{obs}}$. The frequency-integrated flux can be calculated from the intrinsic luminosity, which is what we predict in the GALFORM+UCL-PDR model, and the luminosity distance, D_L ,

$$S_{\text{CO}} = \frac{L_{\text{CO}}}{4\pi D_L^2}. \quad (\text{A2})$$

A widely used luminosity in radio observations is the velocity-integrated CO luminosity, $L_{\text{CO,V}}$. This corresponds to the integral of the monochromatic luminosity over velocity

$$L_{\text{CO,V}} = \int l_\nu(\nu_{\text{rest}}) dV = \frac{c}{\nu_{\text{rest}}} L_{\text{CO}}. \quad (\text{A3})$$

Here c is the speed of light and dV is the differential velocity, which is related to ν_{rest} and ν_{obs} as $dV = c(d\nu_{\text{rest}}/\nu_{\text{rest}}) = c(d\nu_{\text{obs}}/\nu_{\text{obs}})$. Observationally, the velocity-integrated luminosity is calculated from the velocity-integrated flux, $S_{\text{CO,V}} = \int s_\nu(\nu_{\text{obs}}) dV$. We can estimate the observable quantity, $S_{\text{CO,V}}$, from our predicted $L_{\text{CO,V}}$ as,

$$S_{\text{CO,V}} = (1+z) \frac{L_{\text{CO,V}}}{4\pi D_L^2}. \quad (\text{A4})$$

The third widely used luminosity in radio observations is the brightness temperature luminosity. The definition of the rest-frame brightness temperature of an emitting source is

$$T_{\text{B}}(\nu_{\text{obs}}) = \frac{c^2}{2k_{\text{B}}} \frac{s_\nu(\nu_{\text{obs}})(1+z)}{\nu_{\text{obs}}^2 \Omega}. \quad (\text{A5})$$

Here k_{B} is Boltzmann's constant and Ω is the solid angle subtended by the source. The brightness temperature in Eq. A5 is an intrinsic quantity, given that the factor $(1+z)$ converts the brightness temperature from the observer-frame to the rest-frame. In the regime of low frequencies (the Rayleigh-Jeans regime), such for as the rotational transitions of CO, in an optically thick medium and with thermalised CO transitions, the brightness temperature corresponds to the true temperature of the gas. The integrated CO line intensity is defined as the velocity-integrated brightness temperature, $I_{\text{CO}} = \int T_{\text{B}}(\nu_{\text{obs}}) dV$. The brightness temperature luminosity is then defined as

$$L'_{\text{CO}} = I_{\text{CO}} \Omega D_A^2, \quad (\text{A6})$$

where $D_A = D_L(1+z)^2$ is the angular diameter distance and therefore ΩD_A^2 is the area of the source. From Eqs. A2, A5 and A6 it is possible to relate L'_{CO} to L_{CO} ,

$$L'_{\text{CO}} = \frac{c^3}{8\pi k_{\text{B}} \nu_{\text{rest}}^3} L_{\text{CO}}. \quad (\text{A7})$$

By definition, the relation between L'_{CO} and the molecular hydrogen mass is parametrised by the factor α_{CO} ,

$$L'_{\text{CO}} = \frac{M_{\text{H}_2}}{\alpha_{\text{CO}}}. \quad (\text{A8})$$

Note that here we define α_{CO} in terms of molecular hydrogen mass, as done for example by Tacconi et al. (2010) and Genzel et al. (2010). However, other authors define α_{CO} in terms of the total molecular gas mass (e.g. Solomon & Vanden Bout 2005). These two definitions differ by a factor X_{H} , the hydrogen mass fraction.

In Eq. 6 in §2.2 we introduced the relation between I_{CO} and the molecular hydrogen column density N_{H_2} , $X_{\text{CO}} = N_{\text{H}_2}/I_{\text{CO}}$. Given that $M_{\text{H}_2} = m_{\text{H}_2} N_{\text{H}_2} \Omega D_A^2$, where m_{H_2} is the mass of a hydrogen molecule, the relation between α_{CO} and X_{CO} is simply

$$\alpha_{\text{CO}} = m_{\text{H}_2} X_{\text{CO}}. \quad (\text{A9})$$

We can therefore estimate the brightness temperature CO luminosity introduced above from the molecular hydrogen mass, calculated in GALFORM, and the X_{CO} conversion factor calculated in the UCL-PDR model as,

$$L'_{\text{CO}} = \frac{M_{\text{H}_2}}{m_{\text{H}_2} X_{\text{CO}}}. \quad (\text{A10})$$

L_{CO} and $L_{\text{CO,V}}$ are also estimated from M_{H_2} and X_{CO} using Eqs A1, A3, A7 and A10. For a more extended review of all the conversions between units and from CO luminosity to molecular mass, see Appendices A and B in Obreschkow et al. (2009).

To facilitate the comparison with observations, we use $L_{\text{CO,V}}$ to construct the CO luminosity function and L_{CO} to compare against IR luminosity. To construct CO flux density maps in §5, we use the above relations to determine the velocity-integrated line flux, S_V , from M_{H_2} and X_{CO} .

Throughout this paper we make extensive comparisons between the CO and IR luminosities. In GALFORM, we define the total IR luminosity to be an integral over the rest-frame wavelength range 8–1000 μm , which approximates the total luminosity emitted by interstellar dust, free from contamination by starlight. To estimate the IR luminosity, we use the method described in Lacey et al. (2011) and González et al. (2011) (see also Lacey et al. 2012, in prep.), which uses a physical model for the dust extinction at each wavelength to calculate the total amount of stellar radiation absorbed by dust in each galaxy, which is then equal to its total IR luminosity. The dust model assumes a two-phase interstellar medium, with star-forming clouds embedded in a diffuse medium. The total mass of dust is predicted by GALFORM self-consistently from the cold gas mass and metallicity, assuming a dust-to-gas ratio which is proportional to the gas metallicity, while the radius of the diffuse dust component is assumed to be equal to that of the star-forming component, which corresponds to the disk or the bulge half-mass radius depending on whether the galaxy is a quiescent disk or a starburst, respectively. This dust model successfully explains the Lyman-break galaxy LF up to $z \sim 10$ (see Lacey et al. 2011).